Comparison Between the Measured and Calculated Spectral Characteristics of Shortwave Radiation in the Free Atmosphere Over the Desert

(From the Data of the Caenex-70 Expeditions)

By
K.Ya. Kondratyev, R.M. Welch, O.B. Vasiliev, V.F. Zhvalev, L.S. Ivlev and V.F. Rodionov

Department of Atmospheric Science
Colorado State University
Fort Collins, Colorado

This contribution is the second in a series of reports on GATE Radiation Subprogramme results which will be published simultaneously as CSU Atmospheric Science Papers in English and in the Transactions of the Main Geophysical Observatory, Leningrad.
December 1976

Colorado State University

Department of Atmospheric Science

Paper No. 261

COMPARISON BETWEEN THE MEASURED AND CALCULATED SPECTRAL CHARACTERISTICS OF SHORTWAVE RADIATION IN THE FREE ATMOSPHERE OVER THE DESERT (FROM THE DATA OF THE CAENEX-70 EXPEDITIONS)

By

K. Ya. Kondratyev[1,2]

R. M. Welch[3]

O. B. Vasiliev[1]

V. F. Zhvalev[2]

L. S. Ivlev[1]

V. F. Rodionov[1]

1. Department of Atmospheric Physics
Leningrad State University

2. Department of Radiation Studies
Main Geophysical Observatory
7, Karbysheva Street
194018 Leningrad
U.S.S.R.

3. Department of Meteorology
University of Utah
Salt Lake City, Utah 84112

Present Affiliation:

Department of Atmospheric Science
Colorado State University
Fort Collins, Colorado 80523

ATMOSPHERIC SCIENCE PAPER NO. 261

This contribution is one in a series of reports which will be published jointly as an Atmospheric Science Paper, from the Department of Atmospheric Science, Colorado State University, Fort Collins, and in the Transactions of the Main Geophysical Observatory, Leningrad.

December 1976

PREFACE

This joint research report presents the results obtained by the Soviet/American exchange program between the U.S. National Science Foundation and the U.S.S.R. Hydrometeorological Service aimed at studying aerosol and cloud effects upon radiative processes in the real atmosphere as part of working group 8. The team of Soviet scientists from the Main Geophysical Observatory and Leningrad State University, headed by Professor K. Ya. Kondratyev, have supplied field data measured in the CAENEX observational program. A radiative transfer model developed by Dr. Welch has been used for the intercomparison studies between observations and calculations. It is the authors' hope that this timely exchange of scientific results will facilitate research progress in atmospheric radiation studies throughout the world.

ABSTRACT

This report summarizes the results of a joint Soviet/American exchange program to compare calculations with observations in the real atmosphere for determination and study of diabatic processes that are important for tropospheric energetics. Complete spectral measurements of the radiation field and aerosol optical properties under turbid conditions have been supplied. Using these data, radiative transfer calculations have been performed in order to provide an independent check on the accuracy of previous measurements as well as provide recommendations for improved observations.

The effect of a small amount of highly absorbing material, such as hematite, upon the radiation field has been demonstrated. Theoretical results indicate (1) that the effects of variations of the solar zenith angle during observations is not an important consideration, (2) that variations of surface albedo do not contribute significantly to the radiation fields in highly turbid conditions, (3) that ozone absorption variations are not important in the troposphere, and (4) that variations in the size distribution with height were surprisingly ineffective in determining radiation fluxes. On the other hand it was shown that variations in aerosol concentrations had a major impact upon radiation fluxes, and particularly upon the flux divergences.

Extensive data are presented giving spectral shortwave radiation flux and flux divergence values as a function of height in the atmosphere. Furthermore, the complete aerosol data used in the intercomparison studies are also presented along with the theoretical calculations.

It is shown that no "best fit" over all spectral regions was possible. Therefore, further studies have been performed to test the sensitivity of results to small variations in input parameters. It is a normal procedure to assume that contributing aerosol particles share a similar size distribution function, even if variations in height are included. However, preliminary results indicate that it may be necessary to provide size distributions for the various components of aerosol, or at least for such optically active particles as hematite.

TABLE OF CONTENTS

LIST OF TABLES

LIST OF TABLES (Continued)

LIST OF TABLES (Continued)

LIST OF TABLES (Continued)

LIST OF FIGURES

INTRODUCTION

Extensive experimental investigations have been carried out in recent years as part of the Complex Atmospheric Energetics Experiment (CAENEX) program. The data have been obtained from simultaneous surface, airborne, and satellite measurements of the shortwave radiation field for various geographical and atmospheric conditions. In addition, those surface and atmospheric parameters which determine the radiation field have also been measured. From these data taken in the real atmosphere. it is now possible to more fully understand both quantitatively and qualitatively the contribution of shortwave radiation aerosol absorption to the atmospheric heat budget through radiative flux divergences. In particular, previously detected "residual absorption" in those wavelengths where molecular absorption is low has now been identified as absorption of shortwave radiation by aerosol. The radiation measurements during the 1970 CAENEX and the 1974 GATE field observations both showed strong aerosol absorption by ferric oxides.

Detailed analysis of the experimental results can be performed only on the basis of numerical modelling of radiative transfer under measured atmospheric conditions. In order to properly simulate the radiation field observations, it is necessary to develop a theoretical model capable of reasonably accurate reproduction of radiative fluxes, net fluxes and flux divergences.

A great number of different techniques for theoretical description of radiative transfer in the atmosphere are known. As applied to the experimental results of the CAENEX program, it is reasonable to use approximate calculation methods which do not require extensive computer

time since the accuracy of both the measurements of radiative fluxes and flux divergences as well as optical parameters are rather limited.

The present work is the result of combined efforts of Soviet and American specialists brought together through an exchange program between the U.S. National Science Foundation and the U.S.S.R. Hydrometeorological Service. The goals of this exchange program are (a) to calculate spectral radiative fluxes, net fluxes and flux divergences in the free atmosphere from measured optical atmospheric and surface parameters for one of the observational days of the CAENEX program, 25 October 1975, and (b) to compare measured with calculated results. While further and much more extensive intercomparisons are continuing, the purpose of the present paper is to discuss preliminary results along with the specification of the calculational scheme and optical parameters used in this study.

Part I. EXPERIMENTAL DATA

1. Results of the observations of spectral fluxes, net fluxes and radiative flux divergences in the free atmosphere on 25 October 1970.

Experiments included within the "CAENEX-70" program are described in detail in the literature.[1-5] Therefore, the present paper refrains from descriptions of observational technique and data processing. The observational program has been conducted aboard the flying laboratory IL-18 of the Main Geophysical Observatory, Leningrad, over the Kara Kum desert in the Repetek region of the USSR. The 25 October 1970 data were taken both in the surface layer at the ground and in the troposphere from aboard the IL-18 flying laboratory.

In the surface layer the aerosol number density, size distribution, and chemical composition were measured. On board the IL-18 the following observations have been carried out during the CAENEX-70 program:

1. Spectral distribution of upward and downward fluxes of short-wave radiation using a diffraction spectrophotometer, K-2 (spectral range 0.4-0.9μm, spectral resolution 0.02μm; recording time is 10 sec.).
2. Spectral brightness distribution of the surface-atmosphere system in different directions using a prism spectrophotometer, SPI-2M (spectral range 0.4-2.5μm, view angle is 30°; recording time is 10 sec.).
3. Concentrations and size distributions of aerosol particulates using a continuously operating impactor.
4. Spectral transmission of the atmosphere using the infrared-solar spectrometer IRSS-2 (spectral range 2-2.5μm, view angle is 0.5°; recording time is 10 min.).
5. Integral upward and downward long- and short-wave fluxes using pyranometers (spectral range 0.3-3.0μm and 3-30μm, view angle is 180°; time of one measurement is 3 min.).
6. Vertical profiles of temperature, moisture, ozone concentration, and atmospheric pressure.

The Repetek 25 October 1970 observations showed for the first time that aerosols as well as absorption by gases may lead to significant radiative flux divergences in the real atmosphere. In some cases aerosols can absorb energy of similar magnitude as the gaseous components. Figure 1a shows the difference in the net flux between 8.4 and 0.3 km as a function of wavelength for gaseous and aerosol absorption. Figure 1b shows the net flux difference of Figure 1a divided by the average total downward flux for this same height range. The spectral distribution of radiative flux divergence has the same spectral variation as does the

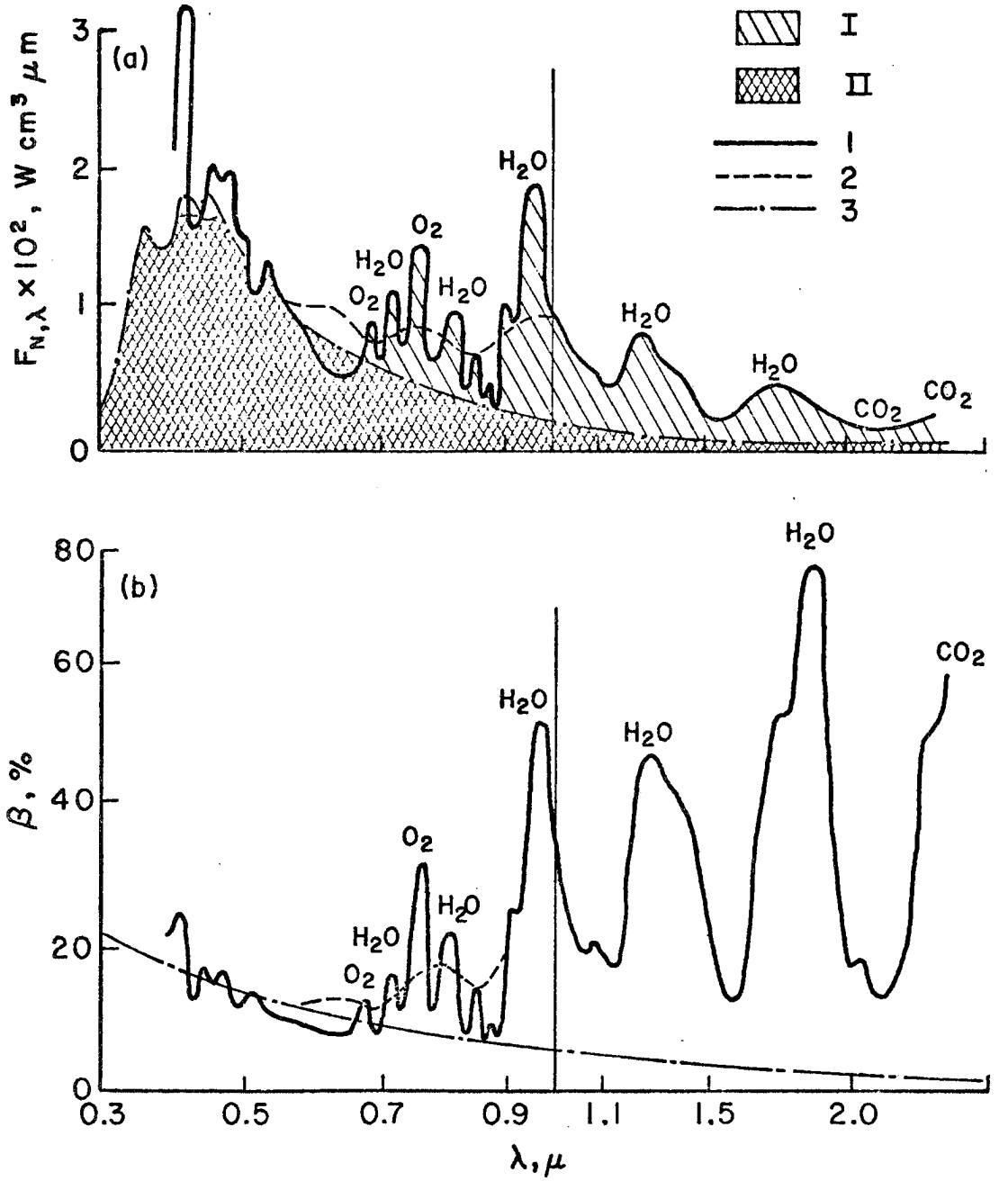

Figure 1. (a) Absolute ($F_{N,\lambda}$) and (b) relative ($\beta = F_{N,\lambda}/F^{\downarrow}$(P-50) · 100%) spectral heat budget in the 0.3 - 8.4 km layer
I - molecular absorption; II - aerosol absorption
1 - observed value of the radiative flux divergence
2 - spectral radiative flux divergence from the SPI-2M spectrometer
3 - spectral variation of aerosol absorption as approximated by the dependence λ^{-1}.

imaginary part of the refractive index of ferric oxide as shown in Figure 2. The hematite component of the aerosol gives the reddish color to desert sand in the Repetek region. It is interesting to note that observations of radiative flux divergences in the town of Shevchenko in 1970 showed that aerosol absorption was highly variable, decreasing in some cases to zero. Its value depends upon the location and conditions under which the aerosol air mass was formed.

The 25 October 1970 observations were statistically processed and smoothed, and atmospheric spectral optical characteristics were constructed at 100 mb intervals (through interpolation from 350 to 950 mb and through extrapolation outside of this interval). These data are given graphically in previous papers.[6-7] In the present work these data are reproduced in Tables 1-6 and are later used for intercomparisons with the calculational results. Observations indicated that under desert conditions the aerosol was mainly generated at the earth's surface and rose to a level of about 500 mb. In the higher layers there must be another source of aerosol since in these layers the optical properties differed considerably from the surface aerosol.

Using the two-flux radiative transfer approximation, extinction and absorption coefficients $\beta_{ext,\,\lambda}$ and $\beta_{abs,\,\lambda}$ and the single scattering albedo $\tilde{\omega}_o$ have been estimated at various heights in the atmosphere.[5,8,9] In these simulations it was found that $\tilde{\omega}_o \leq 0.85\text{-}0.90$ in all cases. Therefore, it becomes clear that pure scattering does not exist in any spectral interval. The given $\tilde{\omega}_o$ estimates, being obtained from approximate calculations, are rather tentative. However, since the true absorption $\beta_{abs,\,\lambda}$ is substantial, the conclusion about the lack of pure scattering is beyond doubt.

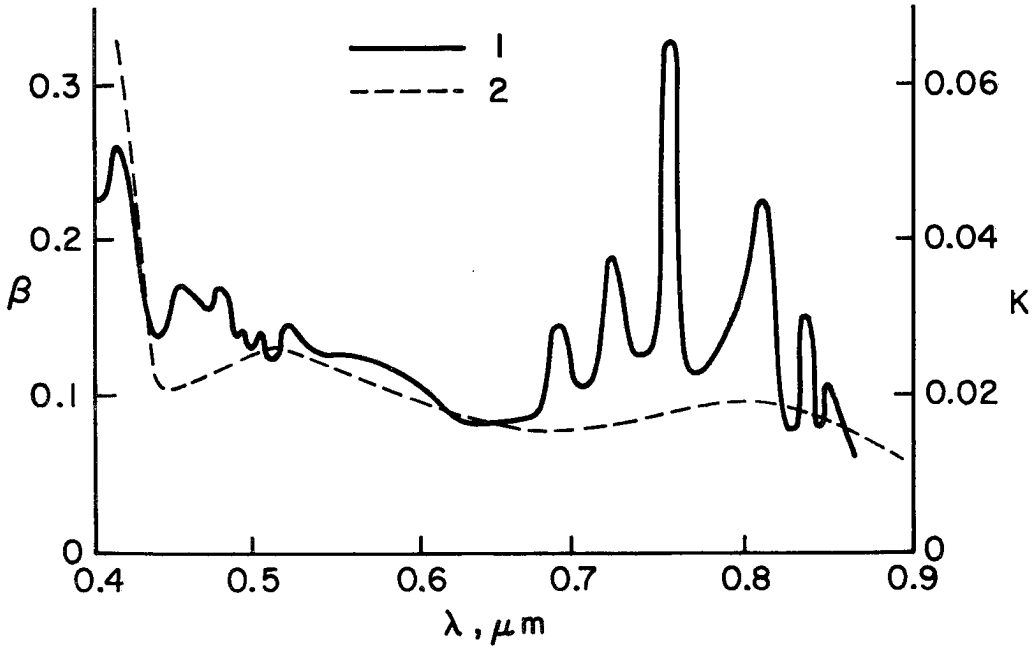

Figure 2. Absolute shortwave spectral heat budget (1) compared with the imaginary part (k) of the complex index of refraction (2) for hematite.

Table 1. Vertical profile of downward radiative spectral flux.

$$F_{\lambda}^{\downarrow} \cdot 10^{4} \ \frac{\text{watts}}{\text{cm}^2 \mu\text{m}}$$

	P(mb)										
λ(μm)	0	100	200	300	400	500	600	700	800	900	1000
0.42	1090	1078	1045	1011	977	939	881	853	799	738	670
0.43	1145	1096	1062	1027	911	950	884	858	800	734	652
0.44	1200	1142	1107	1070	1033	991	927	895	837	768	684
0.45	1244	1197	1162	1124	1085	1042	986	946	888	821	741
0.46	1276	1245	1210	1171	1132	1088	1039	992	936	872	800
0.47	1292	1273	1237	1198	1159	1115	1071	1021	967	907	844
0.48	1287	1273	1238	1199	1160	1117	1076	1025	973	918	862
0.49	1264	1247	1212	1175	1137	1096	1054	1007	957	907	856
0.50	1226	1200	1167	1131	1094	1055	1015	971	924	878	831
0.51	1179	1143	1110	1078	1041	1005	966	927	884	841	797
0.52	1128	1086	1054	1024	989	956	920	885	845	805	764
0.53	1079	1037	1007	978	946	916	882	851	814	777	739
0.54	1036	999	971	944	915	887	856	827	793	759	723
0.55	1000	972	946	919	894	868	840	812	780	748	714
0.56	973	953	928	902	800	855	829	803	772	741	708
0.57	951	937	914	888	869	844	819	794	764	734	703
0.58	932	920	899	874	855	831	807	783	754	724	694
0.59	913	901	811	858	838	814	790	766	739	710	680
0.60	893	879	859	839	816	793	769	745	719	691	662
0.61	872	855	834	817	792	770	746	722	697	670	641
0.62	848	830	809	792	768	746	722	699	675	648	620
0.63	824	805	784	768	745	724	701	679	655	629	601
0.64	800	780	760	744	724	705	683	662	638	613	580
0.65	776	757	739	723	706	688	668	647	624	600	573
0.66	754	735	720	704	689	672	654	635	612	588	562
0.67	734	714	702	687	674	657	641	622	600	576	550
0.68	714	732	721	707	690	671	648	624	592	555	514
0.69	694	673	654	636	617	597	574	552	526	550	471
0.70	674	662	655	642	630	628	602	584	563	540	514
0.71	654	648	640	629	618	627	591	575	556	534	508
0.72	633	610	607	603	596	586	573	557	535	507	472
0.73	613	624	608	606	597	625	576	564	549	532	512
0.74	594	612	593	596	588	616	570	559	547	533	516
0.75	578	569	558	546	534	520	505	488	468	444	416
0.76	564	494	474	453	431	408	384	360	332	303	271
0.77	553	544	540	535	522	513	502	490	473	452	429
0.78	544	557	546	547	542	541	530	521	512	501	489
0.79	536	541	534	532	527	522	515	505	495	482	467
0.80	527	525	522	517	512	504	499	489	476	462	444
0.81	518	509	508	502	497	489	483	473	459	442	422
0.82	506	516	504	492	480	466	452	436	418	398	375
0.83	493	489	484	478	470	457	447	434	418	398	375

Table 1. Vertical profile of downward radiative spectral flux (Continued)

$$F_{\lambda}^{\downarrow} \cdot 10^{4} \ \frac{\text{watts}}{\text{cm}^{2}\,\mu\text{m}}$$

	P(mb)										
λ(μm)	0	100	200	300	400	500	600	700	800	900	1000
0.84	478	466	464	459	455	449	440	431	419	404	387
0.85	464	454	452	447	443	437	429	421	410	398	384
0.86	551	445	442	437	433	427	420	413	404	394	383
0.87	441	439	434	430	425	420	414	407	399	390	380
0.88	436	435	430	426	421	416	410	403	395	385	373
0.89	438	433	430	425	420	416	409	402	390	376	358

Table 2. Vertical profile of upward radiative spectral flux

$$F_{\lambda}^{\uparrow} \cdot 10^{4} \ \frac{\text{watts}}{\text{cm}^2 \mu\text{m}}$$

	P(mb)										
λ(μm)	0	100	200	300	400	500	600	700	800	900	1000
0.42	284	268	253	235	216	194	172	150	122	93	63
0.43	280	265	250	234	216	196	176	153	127	97	64
0.44	285	272	257	242	225	207	187	165	139	110	76
0.45	294	282	268	253	237	220	200	179	154	125	92
0.46	300	288	275	262	246	230	211	190	166	138	106
0.47	300	289	277	264	249	234	215	196	173	146	116
0.48	295	284	273	260	246	232	214	195	174	149	122
0.49	285	275	264	253	239	225	209	192	172	149	123
0.50	275	265	255	244	231	218	203	187	168	147	124
0.51	266	257	246	236	224	211	197	182	165	146	125
0.52	260	250	240	229	218	207	194	180	164	147	127
0.53	255	246	235	225	215	204	192	180	165	148	130
0.54	250	242	231	222	213	203	192	181	167	151	134
0.55	246	238	228	220	212	203	192	182	169	154	137
0.56	240	234	225	218	210	202	192	182	170	155	139
0.57	234	228	221	215	208	200	191	181	169	156	140
0.58	227	221	216	210	204	197	188	179	168	156	141
0.59	219	214	210	204	199	192	185	176	166	155	141
0.60	212	207	203	198	193	187	180	173	164	153	141
0.61	204	200	196	192	187	182	176	170	161	152	141
0.62	198	195	190	186	182	177	172	166	159	150	140
0.63	188	186	183	180	176	172	167	162	155	147	136
0.64	190	187	182	178	175	170	166	161	154	146	136
0.65	188	185	180	176	172	168	163	158	152	144	134
0.66	187	184	179	175	171	166	161	156	146	140	131
0.67	187	183	178	173	169	164	159	153	146	137	127
0.68	185	180	175	171	166	161	156	150	142	133	124
0.69	144	142	140	138	135	133	129	125	120	113	105
0.70	175	171	166	162	158	153	149	143	136	128	119
0.71	167	164	160	156	153	149	145	140	134	196	118
0.72	132	133	133	132	132	130	128	124	120	114	107
0.73	153	151	149	147	144	142	139	136	131	125	117
0.74	148	147	145	143	142	140	137	134	129	124	117
0.75	118	115	112	108	106	102	99	96	92	87	80
0.76	106	102	98	94	91	87	84	79	75	70	64
0.77	142	140	139	138	136	134	132	129	125	120	114
0.78	141	139	137	136	135	133	130	128	124	119	113
0.79	139	137	136	134	132	130	128	125	121	117	111
0.80	136	135	133	131	129	127	125	122	118	114	108
0.81	132	131	129	128	126	124	122	118	115	111	108

Table 2. Vertical profile of upward radiative spectral flux (Continued)

$$F_{\lambda}^{\uparrow} \cdot 10^{4} \frac{\text{watts}}{\text{cm}^{2}\,\mu\text{m}}$$

	P(mb)										
λ(μm)	0	100	200	300	400	500	600	700	800	900	1000
0.82	110	108	105	104	101	100	98	97	95	93	90
0.83	118	116	114	113	112	110	108	105	102	98	94
0.84	124	123	122	120	118	116	114	112	109	104	99
0.85	124	123	121	119	117	116	114	113	108	104	98
0.86	125	123	121	119	117	115	113	113	108	103	98
0.87	125	123	121	119	117	115	113	114	107	103	97
0.88	124	122	120	118	116	114	112	112	106	102	97
0.89	120	118	117	115	113	111	110	107	103	99	95

Table 3. Vertical profile of spectral radiative balance (net flux)

$$F_{N,\lambda} = (F_{\lambda}^{\downarrow} - F_{\lambda}^{\uparrow}) \cdot 10^4 \ \frac{\text{watts}}{\text{cm}^2 \mu\text{m}}$$

λ(μm)	P(mb) 0	100	200	300	400	500	600	700	800	900	1000
0.42	826	809	792	775	759	743	724	700	675	641	604
0.43	849	831	819	793	776	754	731	704	675	636	589
0.44	890	870	850	829	810	785	759	731	699	660	611
0.45	936	916	894	872	851	824	796	767	736	698	652
0.46	978	957	934	910	887	860	832	802	771	736	695
0.47	1005	983	959	934	910	883	885	825	795	762	726
0.48	1001	989	964	939	914	887	859	830	801	770	738
0.49	994	972	947	922	897	871	844	816	788	759	729
0.50	957	935	912	888	862	838	812	786	759	732	704
0.51	908	886	864	842	818	795	771	747	722	696	670
0.52	856	836	815	794	772	750	728	706	683	660	635
0.53	811	791	772	753	732	712	692	672	651	630	608
0.54	776	757	740	721	702	683	665	647	627	608	589
0.55	751	734	718	700	683	665	647	631	612	594	577
0.56	735	719	704	687	670	653	636	620	602	585	569
0.57	724	708	693	677	661	644	628	612	595	578	563
0.58	713	699	683	667	652	635	618	603	586	569	554
0.59	700	686	670	654	639	622	606	590	573	556	541
0.60	684	670	653	637	622	605	589	573	556	539	524
0.61	684	670	653	637	602	586	569	553	537	520	505
0.62	670	651	631	611	592	572	553	533	514	494	474
0.63	624	611	594	578	563	547	531	514	499	483	466
0.64	604	591	576	561	546	532	516	500	484	467	449
0.65	584	573	560	547	533	519	504	489	472	455	436
0.66	566	556	546	534	522	510	495	481	463	445	425
0.67	549	541	533	524	512	501	488	474	456	437	418
0.68	533	527	521	513	503	493	480	468	449	429	414
0.69	549	532	514	447	494	485	473	460	443	422	411
0.70	505	501	497	491	484	475	464	450	435	417	409
0.71	492	488	484	479	472	464	454	436	427	409	404
0.72	479	475	471	465	459	451	440	428	415	404	392
0.73	493	485	476	470	461	452	441	430	418	407	393
0.74	454	448	441	433	424	413	402	387	375	358	345
0.75	440	432	422	414	404	392	379	365	351	333	316
0.76	426	417	408	398	386	374	360	345	330	312	291
0.77	428	420	411	402	393	385	376	366	354	339	323
0.78	411	409	407	404	401	398	393	387	380	372	362
0.79	395	389	380	376	368	359	348	337	322	305	283
0.80	389	385	377	375	370	362	353	344	330	314	294
0.81	382	380	370	374	369	363	356	347	334	320	301
0.82	417	408	399	388	377	365	352	345	322	320	303
0.83	364	363	362	359	356	351	345	337	325	314	300

Table 3. Vertical profile of spectral radiative balance (net flux) (Continued)

$$F_{N,\lambda} = (F_{\lambda}^{\downarrow} - F_{\lambda}^{\uparrow}) \cdot 10^4 \frac{\text{watts}}{\text{cm}^2 \mu\text{m}}$$

	P(mb)										
$\lambda(\mu m)$	0	100	200	300	400	500	600	700	800	900	1000
0.84	351	350	347	346	343	338	332	325	315	306	294
0.85	337	336	334	332	328	324	319	312	304	297	288
0.86	325	323	322	319	315	311	306	301	295	289	282
0.87	316	314	313	309	306	302	298	294	289	284	277
0.88	313	311	309	306	303	300	296	292	287	280	273
0.89	318	317	314	311	309	307	301	297	289	279	266

Table 4. Vertical profile of shortwave heat balance (flux divergence)

$$\Delta F_{N,\lambda}(P+50mb) = [F_{N,\lambda}(P) - F_{N,\lambda}(P+100mb)] \cdot 10^4 \frac{watts}{cm^2 \mu m}$$

	P(mb)									
λ(μm)	50	150	250	350	450	550	650	750	850	950
0.42	153	157	164	172	182	199	223	263	324	399
0.43	180	186	194	204	217	236	264	304	355	472
0.44	200	206	215	226	240	259	285	322	362	481
0.45	214	221	230	240	254	271	294	323	355	447
0.46	226	232	240	250	262	277	295	316	340	396
0.47	234	240	248	256	266	279	292	307	324	350
0.48	237	242	249	257	265	277	286	296	309	316
0.49	234	239	245	252	259	270	276	284	294	294
0.50	226	231	236	242	248	257	262	268	276	277
0.51	217	220	224	229	233	240	243	249	255	258
0.52	207	209	211	214	216	221	223	227	231	236
0.53	196	197	198	200	201	203	204	206	208	213
0.54	186	187	187	187	187	188	188	189	189	192
0.55	177	177	177	176	176	176	176	176	178	176
0.56	170	169	169	169	169	168	168	167	167	166
0.57	164	164	164	164	164	163	163	162	162	161
0.58	161	161	161	161	161	161	160	160	160	159
0.59	160	160	160	160	160	160	160	160	160	159
0.60	162	162	161	161	160	160	160	160	160	160
0.61	162	162	162	162	161	160	162	162	162	162
0.62	184	185	187	190	193	196	199	203	206	210
0.63	154	155	155	156	157	158	162	164	167	170
0.64	140	143	145	148	151	155	159	163	168	173
0.65	121	125	129	135	142	149	153	160	168	177
0.66	98	104	111	120	131	143	145	155	167	179
0.67	77	85	94	106	120	136	135	150	164	179
0.68	62	71	82	95	111	130	195	234	275	318
0.69	158	162	166	172	177	184	191	199	208	217
0.70	55	63	72	84	98	115	116	136	151	169
0.71	159	65	73	82	94	108	113	131	145	162
0.72	63	68	74	82	91	111	141	180	224	280
0.73	67	71	76	81	96	98	109	124	135	150
0.74	68	71	75	80	88	96	108	121	133	148
0.75	65	68	72	77	85	93	106	119	132	148
0.76	150	161	171	180	192	205	219	233	249	266
0.77	49	51	56	62	70	80	93	107	123	142
0.78	37	39	44	50	59	70	83	98	116	135
0.79	26	27	32	39	49	61	74	90	108	129
0.80	14	18	23	30	41	54	67	84	103	124
0.81	11	12	18	26	37	75	98	128	166	212

Table 4. Vertical profile of shortwave heat balance (flux divergence) (Continued)

$$\Delta F_{N,\lambda}(P+50mb) = [F_{N,\lambda}(P) - F_{N,\lambda}(P+100mb)] \cdot 10^4 \frac{watts}{cm^2 \mu m}$$

	P(mb)									
$\lambda(\mu m)$	50	150	250	350	450	550	650	750	850	950
0.82	9	11	17	25	36	134	148	165	182	200
0.83	11	13	19	27	37	96	116	138	163	190
0.84	14	17	22	29	38	47	59	71	84	98
0.85	19	21	26	31	37	45	54	63	73	87
0.86	22	24	28	31	35	41	47	53	61	68
0.87	24	25	27	30	33	37	42	48	55	62
0.88	22	23	24	28	32	38	44	52	62	75
0.89	18	18	20	27	36	40	59	74	93	118

Table 5. Vertical profile of spectral relative absorption.

$$B_\lambda(P) = \frac{\Delta F_{N,\lambda}(P+50mb)}{F^{\downarrow}_{\lambda}(P)}$$

	P(mb)									
λ(μm)	50	150	250	350	450	550	650	750	850	950
0.42	1.40	1.46	1.57	1.62	1.86	2.12	2.53	3.08	4.05	5.30
0.43	1.57	1.70	1.83	1.99	2.19	2.48	2.99	3.54	4.43	6.43
0.44	1.67	1.80	1.94	2.11	2.32	2.61	2.07	3.60	4.32	6.26
0.45	1.72	1.85	1.98	2.14	2.34	2.60	2.98	3.41	3.99	5.44
0.46	1.77	1.86	1.98	2.13	2.31	2.54	2.84	3.19	3.63	1.54
0.47	1.81	1.88	2.00	2.14	2.30	2.50	2.73	3.00	3.35	3.86
0.48	1.84	1.90	2.01	2.14	2.28	2.48	2.66	2.89	3.17	3.44
0.49	1.85	1.92	2.02	2.14	2.28	2.46	2.62	2.82	3.07	3.24
0.50	1.84	1.92	2.02	2.14	2.27	2.44	2.58	2.76	2.98	3.15
0.51	1.84	1.92	2.02	2.12	2.24	2.39	2.52	2.68	2.88	3.07
0.52	1.84	1.92	2.00	2.09	2.18	2.31	2.42	2.56	2.73	2.93
0.53	1.82	1.90	1.27	2.04	2.12	2.22	2.31	2.42	2.55	2.74
0.54	1.80	1.87	1.92	1.98	2.04	2.12	2.20	2.28	2.38	2.53
0.55	1.77	1.82	1.87	1.92	1.97	2.03	2.10	2.16	2.28	2.35
0.56	1.75	1.77	1.82	1.87	1.92	1.96	2.03	2.08	2.16	2.24
0.57	1.72	1.75	1.79	1.85	1.89	1.93	1.99	2.04	2.12	2.19
0.58	1.73	1.75	1.79	1.84	1.88	1.94	1.98	2.04	2.12	2.20
0.59	1.75	1.78	1.82	1.86	1.21	1.96	2.02	2.09	2.16	2.24
0.60	1.81	1.84	1.87	1.92	1.96	2.02	2.08	2.15	2.22	2.32
0.61	1.86	1.89	1.94	1.98	2.03	2.08	2.17	2.24	2.32	2.42
0.62	2.17	2.23	2.31	2.40	2.51	2.63	2.76	2.90	3.05	3.24
0.63	1.87	1.92	1.98	2.03	2.11	2.18	2.31	2.41	2.54	2.70
0.64	1.75	1.83	1.91	1.99	2.08	2.20	2.33	2.46	2.63	2.82
0.65	1.56	1.65	1.74	1.87	2.01	2.16	2.29	2.47	2.69	2.95
0.66	1.30	1.41	1.54	1.70	1.90	2.13	2.22	2.44	2.72	3.04
0.67	1.05	1.19	1.34	1.54	1.78	2.07	2.11	2.41	2.73	3.11
0.68	1.87	0.97	1.14	1.34	1.61	1.94	3.01	3.75	4.64	5.73
0.69	2.28	2.41	2.54	2.70	2.87	3.08	3.33	3.60	3.95	4.34
0.70	0.82	0.95	1.10	1.31	1.56	1.83	1.93	2.32	2.68	3.13
0.71	0.90	1.00	1.14	1.30	1.52	1.72	1.91	2.27	2.60	3.03
0.72	1.00	1.11	1.22	1.36	1.53	1.89	2.46	3.23	4.18	5.52
0.73	1.09	1.14	1.25	1.34	1.51	1.57	1.89	2.19	2.45	2.82
0.74	1.14	1.16	1.26	1.34	1.50	1.56	1.89	2.16	2.43	2.78
0.75	1.12	1.20	1.29	1.41	1.59	1.79	2.10	2.43	2.82	3.33
0.76	2.66	3.26	3.61	3.97	4.45	5.02	5.70	6.47	7.50	8.78
0.77	0.88	0.94	1.04	1.16	1.34	1.56	1.85	2.18	2.60	3.14
0.78	0.68	0.70	0.80	0.91	1.09	1.29	1.57	1.88	2.26	2.70
0.79	0.48	0.50	0.60	0.73	0.93	1.17	1.44	1.78	2.18	2.68
0.80	0.26	0.34	0.44	0.58	0.80	1.07	1.34	1.71	2.16	2.68
0.81	0.21	0.24	0.35	0.52	0.74	1.53	2.03	2.70	3.61	4.80
0.82	0.18	0.21	0.34	0.51	0.75	2.88	3.27	3.78	4.35	5.02

Table 5. Vertical profile of spectral relative absorption (Continued)

$$B_\lambda(P) = \frac{\Delta F_{N,\lambda}(P+50mb)}{F_\lambda^{\downarrow}(P)}$$

	P(mb)									
$\lambda(\mu m)$	50	150	250	350	450	550	650	750	850	950
0.83	0.22	0.26	0.32	0.56	0.78	2.10	2.60	3.17	3.89	4.77
0.84	0.29	0.36	0.47	0.63	0.84	1.05	1.34	1.64	2.00	2.42
0.85	0.41	0.46	0.58	0.69	0.84	1.03	1.29	1.49	1.78	2.08
0.86	0.49	0.54	0.63	0.71	0.81	0.96	1.12	1.28	1.50	1.72
0.87	0.54	0.57	0.62	0.70	0.78	0.88	1.01	1.17	1.37	1.59
0.88	0.50	0.53	0.56	0.66	0.76	0.91	1.07	1.29	1.57	1.95
0.89	0.41	0.42	0.46	0.64	0.86	1.10	1.44	1.84	2.38	3.14

Table 6. Vertical profile of spectral albedo. $A_\lambda \cdot 10^3$

λ(μm)	P(mb) 0	100	200	300	400	500	600	700	800	900	1000
0.42	255	250	243	233	221	207	192	175	148	124	92
0.43	247	242	236	227	218	206	194	179	155	132	102
0.44	242	237	232	225	218	208	198	185	164	142	113
0.45	238	234	230	224	218	210	201	189	172	151	122
0.46	234	231	227	223	217	211	203	191	177	158	130
0.47	229	227	223	220	215	209	202	191	179	161	136
0.48	225	223	220	217	212	207	200	190	179	163	142
0.49	222	220	218	215	211	206	199	190	180	165	147
0.50	224	221	219	216	212	207	201	192	182	169	153
0.51	228	225	223	220	215	211	205	197	187	175	160
0.52	234	232	229	225	221	216	210	204	194	182	167
0.53	240	238	235	231	227	223	217	210	202	191	174
0.54	245	243	240	236	233	228	223	217	209	198	181
0.55	247	245	243	240	236	232	228	222	215	204	188
0.56	247	245	244	241	238	235	231	226	218	209	194
0.57	245	244	242	241	238	236	233	228	221	212	200
0.58	242	241	240	239	238	236	234	229	223	215	205
0.59	240	239	238	238	237	236	234	230	225	218	210
0.60	238	237	237	237	236	236	234	232	228	228	215
0.61	237	237	236	237	236	236	235	234	231	226	220
0.62	237	237	237	237	237	237	236	236	234	225	225
0.63	239	239	238	239	239	239	238	238	237	234	234
0.64	241	241	241	241	241	240	240	240	239	237	228
0.65	245	245	244	244	243	243	242	241	240	238	232
0.66	249	249	248	247	246	245	243	242	240	237	234
0.67	253	252	251	247	248	246	244	242	240	237	234
0.68	256	254	252	251	249	247	245	243	240	236	233
0.69	209	211	213	216	219	221	224	226	229	231	232
0.70	253	252	251	249	247	246	244	242	239	235	231
0.71	250	249	248	247	246	245	244	242	239	235	230
0.72	217	217	218	219	220	221	222	223	224	225	231
0.73	246	246	246	245	245	244	243	242	240	233	233
0.74	248	248	247	247	246	246	245	244	242	239	235
0.75	252	251	250	250	249	248	247	246	244	241	238
0.76	205	206	207	209	212	214	217	221	225	231	241
0.77	235	237	238	240	242	244	245	247	248	245	243
0.78	246	246	259	258	256	254	253	251	249	244	244
0.79	261	259	258	256	255	253	252	251	249	246	245
0.80	258	256	255	254	253	251	250	250	248	246	246
0.81	242	242	242	242	243	243	243	244	246	247	247
0.82	207	208	209	210	211	214	218	222	227	233	248
0.83	253	252	251	251	251	251	251	251	251	251	250
0.84	257	257	256	256	256	256	256	256	256	255	252
0.85	265	265	264	264	263	263	262	262	261	259	255
0.86	274	274	273	273	271	270	269	268	268	263	258
0.87	281	281	280	279	277	276	274	271	268	265	260
0.88	283	282	281	280	278	276	274	271	268	265	262
0.89	276	274	273	271	270	269	268	266	265	264	264

Conclusions derived from the 25 October 1970 observations are confirmed by observations made on 17 June 1970 in the region of the town Shevehenko, USSR. Observations made simultaneously over the land and sea in the region of Krasnovodsk, USSR, on 10 June 1971 provide similar results. In all these cases the total spectral variation of radiative flux divergence was similar. Hence, one may consider that the 25 October 1970 Repetek observations represent shortwave radiative characteristics found over large regions in the Soviet Union with desert conditions. The question of whether these results are representative of desert conditions in other regions of the globe can only be answered with further observations. Nevertheless, GATE results indicate a very strong absorbing aerosol in the Saharan dust which has been identified as hematite. Therefore, the present results should aid the interpretation of the GATE observations.

2. Optical Model of the atmosphere from the results of the 25 October 1970 observations.

Atmospheric conditions in the observational region were characterized by an extensive anticyclonic air mass with weak winds and high air (above 20°C) and soil (up to 40°C) temperatures. The atmosphere was extremely dry with relative humidity never exceeding 31%. Vertical profiles of meteorological variables are given in Table 7, where H is height, P is pressure, t is temperature, μ is relative humidity, and q is specific humidity. The corresponding vertical profile of ozone concentration is given in Table 8. Since only the total ozone content was measured, this table gives values calculated with respect to height using the mean latitudinal ozone distribution curve.[10] Optical

Table 7. Vertical Profile of Various Meteorological Parameters

H(km)	P(mb)	t(°C)	μ(%)	$q(\frac{gm}{kg})$
0	997	26.0	27.0	3.6
0.1	988	16.2	25.7	3.2
0.29	965	14.4	25.5	2.3
0.35	950	13.0	26.9	2.8
0.50	942	12.2	27.8	2.7
0.88	900	9.0	29.7	2.4
1.05	882	7.6	30.5	2.3
1.36	850	6.3	30.7	2.2
1.84	800	4.2	30.9	2.0
1.98	786	3.6	31.0	1.9
2.37	750	1.7	29.1	1.8
2.59	730	0.7	28.0	1.8
3.05	707	-2.1	24.0	1.7
3.14	700	-2.7	23.3	1.6
4.35	600	-10.6	14.0	0.6
5.10	543	-16.0	16.0	0.4
5.73	500	-18.7	17.0	0.25
7.36	400	-30.8	21.0	0.15
7.40	397	-32.2	21.0	0.13
8.29	350	-36.8	23.0	0.092
9.43	300	-42.4	21.5	0.060
10.57	250	-48.0	29.0	0.028
12.36	200	-51.3	19.2	0.026
15.00	126	-56.3	18.0	0.021
16.52	120	-60.6	17.2	0.020
17.00	91.7	-62.1	17.0	0.019
19.00	63.5	-58.1	17.0	0.030
20.78	50.0	-64.0	17.0	0.025

Table 8. Vertical Profile of Ozone Concentration

P(mb)	ω_{oz} $(\frac{cm}{km})$ $\cdot 10^{-2}$
1000	0.221
950	0.216
900	0.218
850	0.223
800	0.229
750	0.235
700	0.240
650	0.276
600	0.290
550	0.310
500	0.395
450	0.446
400	0.519
350	0.589
300	0.612
250	0.698
200	0.850
150	1.140
100	1.710
50	1.920

parameters necessary for numerical calculations were calculated for the 0.4-0.9μm spectral region. Since absorption coefficients were not available in the oxygen and some water vapor bands, the effects of these gases were neglected in the present calculations. Ozone absorption was only included within the Chappius band. Molecular scattering was taken into consideration using Etterman's model.[11]

The primary purpose of the present investigation was to determine the effect of aerosols upon radiation characteristics in the real atmosphere. Since the data are sufficiently complete it became possible to provide calculations which reasonably simulate the experimental conditions.

The aerosol content of such elements as Fe, Ca, and Zn was extremely variable, which points either to the existence of compounds of these elements in the coarse disperse fraction of the aerosol or to the instability of a particle source containing these elements. Chemical composition of the tropospheric aerosol is rather similar to that of the surface aerosol. The main difference in these two regions is a relatively high content of Fe, Al and Mg in the tropospheric aerosol as compared to the surface aerosol (the maximum concentration of Fe compounds was 7 $\mu g/m^3$.) The content of various chemical elements in the atmospheric aerosol is given in Table 9. As a result of extensive aerosol samples and their subsequent analysis, it was established that quartz particles were the main aerosol component in the surface layer.

These aerosol measurements have been carried out during the experiment both in the surface layer at the ground reference point and in the troposphere from aboard the IL-18 flying laboratory. Vertical profiles

of aerosol number density, size distribution, and chemical composition have been obtained.

Table 9. Contents of various elements ($\mu g/m^3$) in the measured aerosol.

	Si	Ca	Fe	Mg	Al	Ni	Cr	Pb	Mn	Cu
Average	13.5	7.2	5.0	2.8	0.9	0.35	0.3	0.3	0.05	0
Minimum Content	12.0	6.5	3.0	0.7	0.6	0.3	0.2	0.2	0.03	0
Maximum Content	15.0	7.8	7.0	5.0	1.2	0.4	0.4	0.4	0.07	0

Assuming that all chemical compounds included in the aerosol composition are uniformly distributed both fractionally and internally and knowing the optical constants of all constituents it is then possible to determine the optical parameters for such aerosol matter. Such calculations were performed for the aerosol model with the following approximate composition: SiO_2 - 35%, SO_4 - 18%, NH_4 - 4%, NO_3 - 1%, CO_3^{+2} - 8%, Fe_2O_3 - 6%, Fe^{-3}(salts) - 1%, Al_2O_3 - 5%, Ca^{+2} - 9%, Cl^{-1} - 4%, Na^+ - 2% K^+ - 1%, crystallized water - 5%, C-O - 1%, and other elements - 1%. The value of the imaginary part of the complex index of refraction for this model is about 0.005 in the wavelength range 0.4 to 0.9 μm. The real part of the complex index of refraction in this region was 1.65. The size distribution of aerosol particles and the vertical concentration profile is given in Table 10.

Table 10. Particle size distribution (μm) of tropospheric aerosol.

Height	Concentration	% of aerosol in various size distribution intervals				
(m)	$N(cm^{-3})$	$r<0.25\mu m$	0.25-0.30	0.30-0.60	0.60-1.20	$r>1.20\mu m$
0	200	0.70	0.14	0.08	0.045	0.035
5500	0.5	0.62	0.19	0.18	0.009	0.002

Using these data and applying Mie theory, phase function, extinction, absorption, and scattering coefficients were then calculated for the surface layer and at the P=500 mb level. It was assumed that these quantities varied linearly in the 1000 - 500 mb layer and were constant with height above this layer. Values of the absorption, scattering and extinction coefficients as a function of wavelength are given in Table 11 for the surface and at a height of 5500 m.

Table 11. Absorption, scattering, and extinction coefficients (in km^{-1} for $N=10^3$ particles/cm^3) as a function of wavelength at H=200 m and 5500 m.

	H=200 m			H=5500 m		
$\lambda(\mu m)$	β_{abs}	β_{scat}	β_{ext}	β_{abs}	β_{scat}	β_{ext}
0.40	0.38	2.42	2.80	0.55	3.80	4.35
0.45	0.32	2.44	2.76	0.60	3.65	4.25
0.50	0.29	2.49	2.78	0.65	3.50	4.15
0.60	0.26	2.49	2.75	0.62	3.30	3.66
0.70	0.25	2.44	2.69	0.40	3.26	3.66
0.80	0.24	2.39	2.63	0.35	3.00	3.35
0.90	0.23	2.44	2.57	0.36	2.84	3.20

From the data of Table 11 it is seen that the absorption, scattering, and extinction coefficients increase with height. This is a result of the fact that the particle size distribution function varies with height. At high altitudes there is an increase in the percentage of large, optically

more active, particles. This phenomenon is related to coagulation of small particles at great heights where particle residence times are larger than in the lower atmospheric layers.

The previously described aerosol model is primarily responsible for the scattering of solar radiation. However, there is a maximum "residual" aerosol absorption due to hematite particles, Fe_2O_3, in wavelength range 0.42-0.45μm. Therefore, for an accurate description of the radiation field, this aerosol component should also be included separately.

In order to calculate the coefficients of absorption, scattering, and extinction due to individual hematite particles not included in the previously described aerosol model, the following assumptions were made: since the measured hematite particle distribution function is narrow with a maximum at about 0.1μm, a delta function size distribution with radius r=0.1μm is used. The corresponding vertical distribution of Fe_2O_3 particle concentration is given in Table 12.

Table 12. Vertical distribution of Fe_2O_3 particle concentration.

H(km)	0	1	2	3	4	5	6	7	8
$N(cm^{-3})$	1000	800	500	300	250	200	100	50	25

The above particle concentration profile was calculated based upon data concerning the profile of mass concentration of Fe_2O_3 in the total aerosol with the above assumption about hematite particle sizes.

Absorption, scattering, and extinction coefficients for Fe_2O_3 are given in Table 13.

Table 13. Absorption, scattering, and extinction coefficients for hematite (in km^{-1} for $N=10^3$ cm^{-3}).

$\lambda(\mu m)$	β_{abs}	β_{scat}	β_{ext}
0.40	0.0245	0.046	0.071
0.45	0.0388	0.121	0.160
0.50	0.0044	0.143	0.147
0.55	0.0039	0.160	0.164
0.60	0.0074	0.194	0.201
0.65	0.0083	0.200	0.208
0.70	0.0020	0.078	0.080
0.80	0.0006	0.029	0.029
0.90	0.0003	0.016	0.016

All of the optical characteristics presented in this section are the initial data used for further calculations and intercomparison. Data on the spectral albedo of the underlying surface needed for the solution to the radiative transfer equation are presented in the column P=1000 mb in Table 6. Spectral data on the extraterrestrial solar radiation entering the earth's atmosphere are presented in the column P=0 mb of Table 1.

To take into account the influence of the various parameters described above, these values were varied within small limits. These variations are described in more detail in the second part of the present report.

Part II. Calculation of Radiation Characteristics of the Atmosphere.

3. Method of Spherical Harmonics.

There are a large number of techniques available for the solution of the radiative transfer equation in the literature. A preliminary report of the International Radiation Commission on "Standard Procedures to Compute Atmospheric Radiative Transfer in a Scattering Atmosphere" gives a rather comprehensive description of the various procedures in

general use. However, intercomparisons of these radiative techniques for accuracy and computer processing time requirements remains incomplete.

Simplified radiation treatments used in general circulation models do not give sufficient accuracy in either a highly polluted or cloudy atmosphere: even if the radiative fluxes at the earth's surface could be determined with reasonable accuracy, flux divergences would remain highly inaccurate. On the other hand, the observational measurements are not sufficiently accurate to warrant extremely precise radiative transfer treatments requiring large amounts of computer time. It is precisely this state of affairs to which the present effort is directed. It is expected that theoretical calculations will help to determine in which areas more thorough measurements are required. Therefore, in the present investigation a reasonably accurate approximate solution of the radiative transfer equation is required including both scattering and absorption in the vertically inhomogeneous atmosphere. A number of theoretical models which meet the above requirements are available. In particular, the adding or doubling method, the discrete-ordinate method, and the spherical harmonics method all provide rapid numerical evaluation and accuracy commensurable with the quality of the input data.

The following description will outline the spherical harmonics approach as developed by Zdunkowski and Korb.[12] This technique has been applied to cloud models by Welch, et al [13] and has been extended to include the infrared window region by Korb et al.[14] In addition, the spherical harmonics approach has also been applied recently by Welch and Zdunkowski,[15] Canosa and Penafiel,[16] Dave and Canosa,[17] and Deuze et al.[18]

It should also be pointed out that the discrete-ordinate approach as developed by Liou[19] leads to the same solution of the radiative

transfer equation when fluxes are calculated as does the spherical harmonics approach.

The mathematical treatment follows the method of Chandrasekhar[21] in which the radiative intensities are expanded into the cosine series in order to remove the azimuthal dependence. Therefore, we begin with the azimuthally independent radiation transfer equation:

$$\mu \frac{dI^{(m)}(\tau,\mu)}{d\tau} = I^{(m)}(\tau,\mu) - \frac{1-k}{2} \int_{-1}^{1} I(\tau,\mu') \sum_{\ell=0}^{N} a_\ell P_\ell(\mu) P_\ell(\mu') \, d\mu'$$

$$- (2-\delta_{o,m}) \frac{1-k}{4\pi} E_o e^{-\tau/\mu_o} \sum_{\ell=0}^{N} a_\ell P_\ell(\mu) P_\ell(\mu_o) (-1)^\ell \qquad (1)$$

where τ - optical depth measured from the top of the atmosphere

μ, μ', μ_o - cosines of the zenith angles of scattered, incident, and direct solar radiative intensities

$I^{(m)}$ - the "m-th" component of intensity expanded in the cosine series

k - total absorption coefficient divided by the total extinction coefficient

a_ℓ - phase function expansion coefficient

$P_\ell(\mu)$ - Legendre Polynomial

E_o - incident intensity of solar radiation at the top of the earth's atmosphere

and $\delta_{o,m}$ Kronecker delta function.

Due to the fact that only fluxes and flux divergences were needed in the present investigation, only the m=o component will be retained.

In the following development the m=o superscript has been deleted for convenience. The angular variables in the phase function are separated using the addition theorem of spherical harmonics.

The radiation intensity was then expanded into a series of Legendre polynomials in order to separate the dependency of optical pathlength and zenith angle

$$I(\tau,\mu) = \sum_{j=o}^{N} I_j(\tau)\, P_j(\mu) \tag{2}$$

In the present study N=3 was chosen. However, this restriction does not influence the generality of the procedure.

The radiative transfer equation now takes the following form after applying the orthogonality condition for Lengendre polynomials

$$\mu \sum_{j=o}^{N} P_j(\mu) \frac{dI_j(\tau)}{d\tau} = \sum_{j=o}^{N} I_j(\tau)\, P_j(\mu) - \frac{1-k}{2} \sum_{j=o}^{N} a_j\, I_j(\tau)\, \frac{2}{2j+1} P_j(\mu) \tag{3}$$

$$- \frac{1-k}{4\pi} E_o\, e^{-\tau/\mu_o} \sum_{j=o}^{N} (-1)^j\, a_j\, P_j(\mu)\, P_j(\mu_o)$$

where a_j are the phase function expansion coefficients. Next the integral operators

$$\int_{-1}^{1} (\text{----})\, \mu^{\ell}\, d\mu \qquad \text{with} \qquad \ell = 0, 1, \text{---}N \tag{4}$$

are applied to equation (3). An alternate scheme is to apply the operators

$$\int_{-1}^{1} (----)\ p_1(\mu)\ d\mu$$

as suggested by Canosa and Penafiel.[16] A matrix differential equation of the following form results

$$\dot{\mathbb{I}} = \mathbb{B}^{-1}\,\mathbb{A}\,\mathbb{I}\,(\tau) + \mathbb{D}\,(\tau)\,e^{-\tau/\mu_o} \tag{5}$$

where $\mathbb{I}$, $\mathbb{B}$, $\mathbb{A}$, and $\mathbb{D}$ are matrix quantities.

In particular for the case N=3 we have

$$\dot{\mathbb{I}}(\tau) = \frac{d\mathbb{I}(\tau)}{d\tau} = \begin{bmatrix} \dot{I}_o(\tau) \\ \dot{I}_1(\tau) \\ \dot{I}_2(\tau) \\ \dot{I}_3(\tau) \end{bmatrix}$$

where $\mathbb{A}$ and $\mathbb{B}$ are constant matrices. The formal solution to equation (5) is given by

$$\mathbb{I}(\tau) = e^{-\mathbb{B}^{-1}\mathbb{A}\tau}\,\mathbb{C} + \int_0^{\tau} e^{-\mathbb{B}^{-1}\mathbb{A}(\tau-s)}\,e^{-s/\mu_o}\,\mathbb{D}\,ds = \mathbb{N}(\tau)\,\mathbb{C} + \mathbb{H}(\tau) \tag{6}$$

where

$$\mathbb{C} = \begin{bmatrix} C_o \\ C_1 \\ C_2 \\ C_3 \end{bmatrix}$$

are the integration constants.

The evaluation of the exponential matrices follows the method of Putzer.[27] In addition a complete analysis and analytical solution for

k=o (absorption) and k≠o (non-absorption) in both resonance and non-resonance cases is given by Zdunkowski and Korb.[12]

In the case of N=3 the integration constants of the general solution are found by specifying the mean intensity and flux for upward and downward radiation both at the top of the earth's atmosphere and at the surface. The mean intensity ($\bar{I}$) and flux (F) are recognized as the zeroth and first statistical moments of radiative intensity and may be given in the following form:

For upward radiation

$$M_1^{(o)}(\tau) = 2\pi \int_0^1 I(\tau,\mu)\, \mu^o\, d\mu = 2\pi\, \bar{I}_1(\tau)$$

$$M_1^{(1)}(\tau) = 2\pi \int_0^1 I(\tau,\mu)\, \mu^1\, d\mu = F_1(\tau)$$

For downward radiation

$$M_2^{(o)}(\tau) = 2\pi \int_{-1}^0 I(\tau,\mu)\, \mu^o\, d\mu = 2\pi\, \bar{I}_2(\tau)$$

$$M_2^{(1)}(\tau) = 2\pi \int_{-1}^0 I(\tau,\mu)\, \mu^1\, d\mu = -F_2(\tau)$$

Further we considered a horizontally homogeneous atmosphere above a diffusely reflecting surface of uniform albedo which is illuminated by parallel solar radiation. Using the above expressions, the boundary conditions take the following form:

Top of the atmosphere, $\tau=0$:

$$M_2^{(0)}(0) = 0$$

$$M_2^{(1)}(0) = 0$$

Earth's surface, $\tau=T$:

$$M_1^{(0)}(T) = 2M_1^{(1)}(T)$$

$$M_1^{(1)}(T) = A_s\left(-M_2^{(1)}(T) + \mu_0 E_0 e^{-T/\mu_0}\right)$$

When a vertically inhomogeneous atmosphere is considered, then boundary conditions are required at each interface. The zeroth and first statistical moments of radiative intensity are required to be continuous for both upward and downward radiation at each interface.

Previous studies[13-15] have indicated that radiative fluxes are accurate to within 1-2% and that flux divergences are accurate to within 10-15%.

4. Preliminary Results of Calculations

The present investigations use 10 horizontally homogeneous vertical layers. Within each layer, all input data is assumed constant with height. Input parameters include: aerosol absorption and extinction coefficients (km^{-1}), Rayleigh scattering coefficients (km^{-1}), phase functions, aerosol concentrations ($particles/cm^3$), water vapor density (gm/cm^3), ozone concentration (cm/km), pressure (mbar), incident solar flux ($watts/cm^2\mu m$), surface albedo (%), zenith angle, and wavelength.

Output (calculated) data include downward and upward diffuse flux, total downward flux, net flux, and flux divergence.

Several calculations were made in order to obtain a preliminary "best fit" with observations and to determine the contributions of various input parameters. However, the primary purpose of these preliminary calculations is to properly account for the large absorption observed in the hematite region 0.42-0.45μm where there is no gaseous absorption. Intercomparison of calculations and measurements for three wavelengths (0.45, 0.60, and 0.85μm) and two atmospheric levels (P= 0 and 1000 mb) is shown in Table 14. It should be remembered that measurements are estimated to be accurate to within 2-5% for fluxes and 30-40% for flux divergences.

The first calculation assumed an aerosol primarily of SiO_2 (Table 9) which had small absorption coefficients: this will be called the "mean" aerosol in subsequent discussion. The calculations gave poor agreement with observations, particularly in the region 0.42-0.45μm. The experimental data refer to the layer from 350 to 950 mb. Observed values given in Table 14 for 1000 and 0 mb have been extrapolated below 950 mb and above 350 mb. The second theoretical study used the same aerosol concentration as before but arbitrarily increased the absorption parameters by a factor of three. In this case, much better agreement was obtained between observations and calculations, particularly for wavelengths $\geq$ 0.60μm. However, these intercomparisons showed that absorption would have to be mulitplied by a factor of 4 or 5 to obtain any kind of reasonable agreement in the strong hematite region, 0.45μm. Therefore, it seems clear that SiO_2 and other low-absorption aerosols are not of primary importance in determing the characteristics in the

Table 14. Radiation fluxes for various calculational models at the top of the atmosphere and at the surface.

$$\left(\frac{\text{watts}}{\text{cm}^2\,\mu\text{m}} \cdot 10^4\right)$$

$\lambda(\mu m)$	P(mb)	Observed values $F^{\uparrow}$	$F^{\downarrow}$	F_N	"mean" aerosol $F^{\uparrow}$	$F^{\downarrow}$	F_N	"mean" aerosol with absorption increased X3 $F^{\uparrow}$	$F^{\downarrow}$	F_N
0.45	0	294	1244	930	348	1247	899	301	1246	945
	1000	92	741	651	119	955	836	109	879	770
0.60	0	212	893	681	239	895	692	203	895	692
	1000	141	662	521	163	755	592	152	706	554
0.85	0	124	464	340	132	465	333	113	465	352
	1000	98	384	284	107	420	313	100	395	295

$\lambda(\mu m)$	P(mb)	Hematite alone $F^{\uparrow}$	$F^{\downarrow}$	F_N	aerosol scattering hematite absorption $F^{\uparrow}$	$F^{\downarrow}$	F_N	aerosol and hematite scattering and absorption $F^{\uparrow}$	$F^{\downarrow}$	F_N
0.45	0	355	1247	892	265	1246	981	400	1248	848
	1000	96	763	667	107	861	754	83	656	573
0.60	0	319	896	577	239	896	656	329	896	567
	1000	144	658	514	164	759	595	125	571	446
0.85	0	126	465	339	145b	479	334	148	465	317
	1000	114	452	338	112	445	333	98	380	282

0.4-0.5μm wavelength region. Within this spectral interval aerosols may have their maximum impact upon the radiative heat budget since the solar intensity reaches a maximum in this region.

The third model assumed only the hematite (Fe_2O_3) aerosol which has strong absorption properties in the visible part of the spectrum. The hematite calculations showed better agreement with observations, indicating that the very strong absorption in the region 0.4-0.5μm is largely due to this aerosol. Actual data indicate absorption exceeding 20% near 0.45μm. It appears safe to conclude that hematite has the greatest impact upon solar radiation in the spectral region 0.4-0.5μm for these observations. However, in the Near-Infrared regions without gaseous absorption (0.75-0.90μm), the SiO_2-type of aerosol gave better agreement with measurements than did hematite alone.

Since both hematite and other aerosols coexist in the atmosphere, the next investigations included both sources. The fourth model included hematite and "mean aerosol" absorption and "mean aerosol" scattering, neglecting hematite scattering. The fifth model included both hematite and "mean aerosol" absorption and scattering. While these latter two models provide a better average fit over all wavelength intervals, it can be seen that no one model is completely adequate in all spectral intervals.

The worst percentage agreement in net flux divergences occurred in the region between 0-500 mb where experimental data on aerosol parameters are non-existent. It seems either that a much larger aerosol absorption/extinction ratio exists in this region or that extrapolations of flux measurements from the lower atmosphere are in error.

In subsequent analysis, only the first, fourth, and fifth schemes of Table 14 will be used (renamed Models I, II, and III). Results of calculations for these models are given in Tables 15-27, and should be compared with Tables 1-6. More detailed discussion is found in the next section.

Part III. COMPARISON BETWEEN THE CALCULATED AND EXPERIMENTAL DATA

5. Comparison between the calculated and measured radiation characteristics of the free atmosphere for three models.

The intercomparison between the experimental and calculated data should begin with the comparison between the adopted optical model of the atmospheric aerosol and the optical characteristics calculated by an approximate formula.[9-10] Figure 3 shows curves of the absorption coefficient β_{abs}, and Figure 4 shows the corresponding curves of the extinction coefficient β_{ext} obtained from the 25 October 1970 data. To calculate optical characteristics, it is necessary to multiply the corresponding coefficients of Tables 11 and 13, by particle concentrations from Tables 10 and 12 for three atmospheric levels corresponding to 500, 700, and 900 mb (for which reliable measurements are available).

Inspection of Figure 3 shows that the absorption coefficients used in Models II and III and similar to those obtained from the approximate formula in the hematite absorption region. Agreement is better in the region below 700 mb. As to the extinction coefficient, values obtained from the approximate formula[9-10] are between the values corresponding to Models II and III. The difference between calculated and observed extinction coefficients is about a factor of 2. As will be seen from further comparisons, a model intermediate between Models II and III gives best agreement.

Table 15. Vertical profiles of downward spectral flux. Model I

$$F^{\downarrow} \cdot 10^4 \ \frac{\text{watts}}{\text{cm}^2 \mu\text{m}}$$

	P(mb)										
λ(μm)	0	100	200	300	400	500	600	700	800	900	1000
0.42	1093	1074	1074	1065	1053	1025	968	939	906	862	788
0.43	1148	1127	1127	1118	1107	1080	1030	999	964	918	844
0.44	1203	1184	1182	1172	1161	1137	1089	1062	1025	981	904
0.45	1247	1228	1221	1211	1200	1180	1138	1112	1076	1030	955
0.46	1279	1260	1248	1237	1226	1210	1173	1147	1115	1068	990
0.47	1291	1276	1262	1251	1239	1225	1193	1168	1133	1090	1013
0.48	1290	1271	1255	1245	1233	1222	1193	1170	1137	1095	1020
0.49	1267	1248	1233	1222	1212	1202	1177	1155	1124	1082	1012
0.50	1229	1211	1196	1186	1175	1167	1147	1126	1098	1060	991
0.51	1182	1164	1149	1140	1130	1123	1105	1086	1059	1023	958
0.52	1130	1113	1098	1089	1081	1075	1059	1042	1016	983	922
0.53	1081	1064	1051	1042	1034	1029	1015	999	976	943	887
0.54	1038	1022	1008	1001	994	989	976	962	933	910	856
0.55	1002	986	973	966	960	955	944	930	910	882	853
0.56	975	959	948	940	934	930	919	906	887	860	811
0.57	953	937	926	919	913	910	900	887	868	843	796
0.58	934	918	907	901	895	892	883	871	853	828	782
0.59	915	899	889	883	877	874	866	854	837	813	769
0.60	895	879	869	864	859	856	848	837	820	797	755
0.61	874	860	850	846	841	838	830	820	804	782	741
0.62	850	837	829	824	820	818	810	800	786	764	725
0.63	826	814	807	803	799	797	790	781	767	746	711
0.64	802	792	785	781	778	776	770	761	747	727	693
0.65	778	769	763	760	756	755	749	740	727	709	676
0.66	756	748	742	739	736	735	729	721	709	691	659
0.67	736	728	723	721	718	717	711	704	692	674	644
0.68	716	709	705	702	700	698	693	686	674	658	628
0.69	696	689	686	684	682	680	675	668	658	641	612
0.70	676	670	667	665	663	662	657	651	640	624	597
0.71	655	650	647	645	644	643	638	632	621	606	580
0.72	634	630	627	625	623	622	618	612	602	587	562
0.73	614	610	607	606	604	603	599	593	584	569	545
0.74	595	591	589	587	586	585	581	575	566	552	529
0.75	579	575	573	572	570	569	566	560	552	538	516
0.76	565	561	559	558	557	556	552	547	539	526	504
0.77	554	550	549	547	546	545	542	537	529	516	495
0.78	545	542	540	539	538	537	534	529	522	508	487
0.79	537	534	532	531	530	529	526	521	513	501	481
0.80	528	525	524	523	522	522	518	514	506	494	474
0.81	519	516	515	514	513	513	510	505	498	486	467
0.82	507	504	503	502	502	501	498	494	486	475	456
0.83	494	491	490	490	489	488	485	481	474	463	445
0.84	479	476	476	475	474	473	471	467	460	450	432

Table 15. Vertical profiles of downward spectral flux. Model I (Continued)

$F^{\downarrow} \cdot 10^4 \frac{\text{watts}}{\text{cm}^2 \mu\text{m}}$

	P(mb)										
λ(μm)	0	100	200	300	400	500	600	700	800	900	1000
0.85	465	463	462	461	460	460	457	453	447	437	420
0.86	452	450	449	448	448	447	444	441	434	425	408
0.87	442	440	439	438	438	437	435	430	422	416	400
0.88	437	435	434	433	433	432	430	426	420	411	396
0.89	439	437	436	435	435	434	432	429	423	413	398

Table 16. Vertical profiles of downward spectral flux. Model II

$$F^{\downarrow} \cdot 10^4 \ \frac{\text{watts}}{\text{cm}^2 \mu\text{m}}$$

	P(mb)										
λ(μm)	0	100	200	300	400	500	600	700	800	900	1000
0.42	1093	1025	983	959	935	915	861	823	766	690	583
0.43	1148	1077	1034	1000	985	967	908	868	806	721	609
0.44	1200	1130	1086	1062	1037	1018	957	914	845	721	636
0.45	1248	1172	1127	1098	1089	1062	1001	949	877	781	656
0.46	1280	1204	1161	1137	1114	1095	1040	1988	916	831	699
0.47	1296	1228	1180	1157	1135	1169	1164	1114	1048	862	734
0.48	1291	1225	1180	1159	1138	1120	1012	1025	960	879	760
0.49	1268	1205	1163	1144	1125	1110	1066	1023	962	886	775
0.50	1230	1170	1132	1115	1097	1087	1049	1010	954	887	782
0.51	1182	1125	1087	1072	1056	1046	1010	980	919	850	755
0.52	1131	1076	1041	1026	1010	1001	968	933	982	816	725
0.53	1082	1029	996	981	967	958	927	895	846	783	697
0.54	1039	987	955	942	929	921	892	860	814	754	672
0.55	1003	953	922	909	896	890	858	832	796	730	651
0.56	975	927	897	885	872	865	838	809	765	709	632
0.57	953	900	876	864	852	845	815	790	747	690	615
0.58	935	887	859	847	835	828	802	773	730	675	600
0.59	916	869	841	829	818	811	785	756	714	659	586
0.60	896	849	822	811	800	793	767	739	697	640	571
0.61	875	830	805	794	784	777	752	725	684	630	560
0.62	851	808	784	774	764	757	734	707	667	616	548
0.63	826	786	764	754	745	738	715	689	652	603	540
0.64	802	764	742	734	725	719	697	671	635	586	525
0.65	778	742	721	714	705	700	678	654	618	571	512
0.66	756	722	703	696	688	683	660	641	609	567	511
0.67	736	704	687	680	673	668	651	630	601	563	512
0.68	716	687	669	663	656	652	638	620	594	559	512
0.69	696	667	652	640	640	636	624	609	586	555	511
0.70	676	649	635	630	624	621	611	597	577	550	510
0.71	656	631	616	612	606	604	594	581	562	537	499
0.72	635	610	597	592	587	585	576	564	548	523	488
0.73	615	591	579	574	570	567	559	548	533	510	476
0.74	596	572	561	557	552	550	543	533	518	498	466
0.75	580	557	546	542	538	536	529	520	506	487	457
0.76	565	544	534	530	526	524	517	509	496	477	448
0.77	554	533	523	520	516	514	508	500	486	469	442
0.78	545	525	515	512	508	506	498	492	480	463	435
0.79	537	517	508	504	501	499	498	486	474	457	431
0.80	528	510	500	497	494	492	486	479	468	452	426
0.81	519	500	492	489	486	484	478	471	460	445	420
0.82	507	489	480	478	474	473	467	461	450	436	411
0.83	494	477	469	466	462	461	455	449	439	425	402
0.84	479	463	454	452	448	447	441	436	426	413	391
0.85	465	449	441	439	436	434	430	424	415	402	380
0.86	452	437	429	426	424	422	418	413	404	391	371
0.87	442	427	420	417	415	413	409	404	395	383	363
0.88	437	423	415	413	410	409	404	399	392	380	360
0.89	439	425	417	415	412	411	407	402	394	382	352

Table 17. Vertical profiles of downward spectral flux, $F^{\downarrow} \cdot 10^4$ $\frac{\text{watts}}{\text{cm}^2 \mu\text{m}}$

	P(mb)										
λ(μm)	0	100	200	300	400	500	600	700	800	900	1000
0.42	1092	1066	1033	1014	992	973	940	905	860	800	703
0.43	1147	1121	1088	1068	1048	1034	995	959	912	855	746
0.44	1202	1176	1143	1123	1103	1080	1052	1014	970	904	791
0.45	1246	1220	1186	1169	1150	1138	1098	1061	1009	946	828
0.46	1278	1253	1222	1205	1187	1175	1138	1102	1052	992	880
0.47	1294	1270	1242	1226	1209	1198	1164	1131	1085	1023	923
0.48	1289	1267	1242	1227	1212	1202	1172	1142	1100	1044	952
0.49	1266	1246	1224	1212	1198	1189	1162	1136	1100	1053	969
0.50	1229	1210	1192	1181	1171	1162	1140	1118	1088	1046	975
0.51	1182	1163	1136	1126	1119	1119	1098	1078	1050	1011	943
0.52	1130	1112	1096	1087	1078	1071	1053	1035	1008	972	907
0.53	1081	1064	1048	1040	1032	1026	1010	992	967	933	873
0.54	1038	1021	1007	1999	991	986	972	955	932	900	843
0.55	1002	985	972	965	958	953	940	924	902	872	818
0.56	975	958	946	939	932	927	915	900	879	849	797
0.57	953	937	924	918	911	907	895	880	865	831	780
0.58	934	917	906	900	893	889	877	863	843	815	765
0.59	915	898	888	881	875	871	860	846	826	798	750
0.60	895	878	868	862	856	853	842	828	809	781	734
0.61	874	859	849	844	838	835	825	812	793	766	720
0.62	850	837	828	822	818	815	805	792	774	748	704
0.63	826	814	805	801	797	794	784	773	755	731	690
0.64	802	791	783	779	775	773	764	753	736	712	672
0.65	778	768	761	758	754	752	744	733	716	693	655
0.66	756	747	741	738	735	732	725	714	700	678	638
0.67	736	728	722	719	716	714	708	698	684	664	623
0.68	716	708	704	701	698	695	691	682	668	649	607
0.69	696	689	685	683	681	675	673	665	653	635	591
0.70	676	670	666	664	663	660	656	649	638	620	576
0.71	655	650	647	645	643	642	637	630	619	603	576
0.72	634	629	626	625	623	622	618	611	600	585	559
0.73	614	610	607	605	604	603	599	592	582	568	542
0.74	595	591	588	587	585	584	580	574	565	551	527
0.75	579	575	573	572	570	568	566	560	551	537	514
0.76	565	561	559	558	557	556	552	547	538	525	503
0.77	554	550	548	547	546	545	542	537	528	516	494
0.78	545	542	540	538	538	536	533	528	520	508	486
0.79	537	534	532	531	530	529	526	521	513	501	480
0.80	528	525	524	523	522	521	518	513	505	494	473
0.81	519	516	515	514	513	512	510	505	497	486	466
0.82	507	505	503	502	501	500	498	493	486	475	455
0.83	494	491	490	489	489	488	485	481	474	464	444
0.84	479	477	475	474	474	473	470	466	460	449	431
0.85	465	463	461	461	460	459	457	453	446	437	419
0.86	452	450	449	448	447	447	444	440	434	425	408
0.87	442	440	439	438	438	437	435	431	425	416	399
0.88	437	435	434	433	433	432	430	426	420	411	395
0.89	439	437	436	435	435	434	432	428	422	414	400

Table 18. Vertical profiles of upward spectral flux. $F^{\uparrow} \cdot 10^4$ $\frac{\text{watts}}{\text{cm}^2 \mu\text{m}}$
Model I.

	P(mb)										
λ(μm)	0	100	200	300	400	500	600	700	800	900	1000
0.42	323	306	309	300	288	260	209	180	152	118	74.9
0.43	333	317	317	308	297	271	222	198	166	131	88.6
0.44	343	326	326	316	306	280	236	213	182	147	104
0.45	348	332	326	316	305	286	247	225	194	160	119
0.46	354	338	329	318	308	292	257	235	209	172	136
0.47	354	339	327	317	306	288	262	242	213	180	140
0.48	349	334	322	312	301	290	264	244	217	185	147
0.49	338	325	312	302	292	283	260	242	217	187	151
0.50	324	312	300	290	282	275	255	239	216	187	153
0.51	312	300	288	280	272	266	249	234	213	186	155
0.52	298	288	276	269	261	256	242	228	209	184	156
0.53	284	275	264	258	251	247	235	222	204	181	156
0.54	273	265	255	249	243	239	229	218	206	180	156
0.55	264	256	247	242	236	233	224	214	199	179	157
0.56	258	251	242	237	232	230	222	212	197	179	158
0.57	253	246	239	234	230	227	220	211	197	179	160
0.58	248	242	235	231	227	225	217	209	187	179	161
0.59	244	238	232	228	224	222	216	208	196	179	162
0.60	239	234	228	224	221	219	214	206	195	179	163
0.61	236	231	226	222	219	217	212	205	194	179	164
0.62	232	227	222	219	216	215	210	203	193	178	164
0.63	228	224	220	217	214	212	208	202	192	178	167
0.64	218	214	210	207	204	203	199	193	183	170	158
0.65	213	209	205	203	201	220	195	190	180	168	157
0.66	208	204	201	199	197	195	191	186	177	164	155
0.67	202	199	195	193	191	190	186	181	173	161	151
0.68	196	192	189	188	186	185	181	176	168	156	147
0.69	190	186	183	182	180	179	175	171	162	152	142
0.70	183	180	177	176	175	173	170	165	158	147	138
0.71	177	174	172	170	169	168	164	160	152	142	134
0.72	171	168	166	165	164	163	160	155	148	138	130
0.73	167	164	162	161	160	158	156	151	145	135	127
0.74	162	160	158	156	155	154	152	148	142	132	125
0.75	159	156	154	154	152	152	149	145	139	130	123
0.76	156	154	152	151	150	149	147	143	137	129	122
0.77	153	151	149	149	148	147	144	141	136	127	120
0.78	151	149	147	146	146	145	142	139	133	125	119
0.79	149	147	146	145	144	143	141	138	132	124	118
0.80	147	146	144	144	143	142	139	136	131	123	116
0.81	145	143	142	141	141	140	138	134	129	122	115
0.82	142	140	139	138	138	137	135	132	127	119	113
0.83	139	137	136	136	135	134	132	129	124	117	111
0.84	135	134	133	132	132	131	129	126	121	114	109
0.85	132	131	129	129	129	128	126	124	119	112	107
0.86	129	128	127	127	126	126	124	121	117	110	105
0.87	127	126	125	124	124	124	122	119	115	109	104
0.88	126	125	124	124	123	123	121	118	114	108	104
0.89	127	126	125	125	124	124	122	120	116	109	105

Table 19. Vertical profiles of upward spectral flux. $F^{\uparrow} \cdot 10^4$ $\frac{\text{watts}}{\text{cm}^2 \mu\text{m}}$
Model II

	P(mb)										
λ(μm)	0	100	200	300	400	500	600	700	800	900	1000
0.42	354	318	282	263	249	230	192	164	127	85.6	56.4
0.43	371	334	296	278	264	246	206	177	138	93.8	65.0
0.44	388	350	317	298	280	261	217	190	150	103	74.9
0.45	400	361	327	309	292	270	233	202	160	110	83.1
0.46	419	379	346	329	311	294	254	222	178	126	94.1
0.47	433	393	362	345	328	312	268	240	195	141	103
0.48	441	398	372	356	340	326	284	256	211	156	111
0.49	442	405	378	363	348	336	296	269	224	168	118
0.50	440	404	380	366	352	345	314	283	238	180	123
0.51	424	390	366	354	341	334	306	276	234	179	124
0.52	406	374	352	345	328	323	297	269	228	176	124
0.53	389	356	338	326	316	311	288	261	223	173	124
0.54	374	345	326	315	305	301	276	255	218	171	125
0.55	362	334	315	306	297	294	270	250	215	169	125
0.56	354	327	309	300	291	288	269	246	212	167	125
0.57	347	322	304	295	287	284	262	243	210	166	126
0.58	341	317	299	291	283	280	262	240	207	165	126
0.59	335	312	295	287	279	276	259	237	205	163	126
0.60	329	306	289	282	274	272	252	234	203	161	125
0.61	323	301	285	278	271	269	249	231	201	160	126
0.62	316	295	280	273	266	264	244	227	208	159	126
0.63	308	287	273	266	260	257	241	222	194	157	129
0.64	297	277	263	257	251	248	230	214	186	150	122
0.65	290	270	257	252	246	243	227	209	183	148	121
0.66	277	258	246	240	235	233	216	203	179	146	122
0.67	264	245	235	229	225	222	208	195	174	144	122
0.68	251	233	222	218	213	211	199	187	168	142	121
0.69	238	218	211	207	202	200	191	180	162	139	120
0.70	224	207	198	195	191	189	180	172	157	136	119
0.71	215	199	190	187	183	182	174	165	151	132	116
0.72	206	191	183	179	176	174	168	159	146	129	114
0.73	198	183	176	173	170	168	162	156	142	126	112
0.74	191	177	170	166	164	162	156	149	138	123	111
0.75	185	171	164	161	159	157	152	145	135	121	110
0.76	180	167	160	158	155	154	149	143	133	120	109
0.77	177	163	157	155	152	151	145	140	131	118	108
0.78	173	160	154	151	149	148	143	138	129	116	107
0.79	170	157	152	149	147	146	141	136	127	116	106
0.80	168	155	149	147	145	143	139	134	126	115	106
0.81	164	152	147	144	142	141	137	132	124	113	104
0.82	160	148	143	141	139	138	134	129	121	111	103
0.83	156	145	140	138	135	134	130	126	119	109	101
0.84	152	141	136	134	132	131	127	123	116	106	99.2
0.85	148	137	132	130	128	127	124	120	113	104	97.7
0.86	144	134	129	127	126	125	122	117	111	103	96.3
0.87	141	131	127	125	123	122	119	116	109	101	95.1
0.88	140	130	125	124	122	121	118	115	109	101	94.9
0.89	141	131	126	125	123	122	119	116	110	102	96.3

Table 20. Vertical profiles of upward spectral flux. $F^{\uparrow} \cdot 10^4$ $\frac{\text{watts}}{\text{cm}^2 \mu\text{m}}$
Model III

	P(mb)										
λ(μm)	0	100	200	300	400	500	600	700	800	900	1000
0.42	256	238	212	196	180	164	140	122	101	80	66
0.43	255	237	212	201	180	165	144	126	107	88	78
0.44	252	236	211	196	181	168	148	132	115	97	91
0.45	245	230	207	193	179	166	150	136	121	105	102
0.46	264	250	227	213	200	187	171	156	140	121	116
0.47	281	267	245	232	220	208	191	175	157	137	127
0.48	294	280	260	249	237	226	208	193	174	152	137
0.49	303	290	273	262	252	242	225	209	189	165	144
0.50	311	298	284	275	266	257	240	224	204	178	151
0.51	298	287	274	266	257	250	235	221	201	177	152
0.52	286	275	263	256	248	242	229	216	197	175	153
0.53	273	264	252	246	239	234	223	211	194	173	153
0.54	262	254	244	238	232	227	217	206	191	172	154
0.55	253	246	237	231	226	222	214	204	190	172	155
0.56	245	239	230	226	220	217	209	200	187	170	156
0.57	239	233	225	220	216	213	206	197	186	170	157
0.58	233	227	220	216	212	209	203	195	184	167	158
0.59	227	222	215	211	207	205	200	192	182	168	158
0.60	220	216	210	206	203	201	196	189	180	166	158
0.61	217	213	207	204	201	199	194	188	179	166	159
0.62	213	209	204	201	198	196	192	186	178	165	159
0.63	210	206	201	198	196	194	190	185	176	165	162
0.64	199	196	191	189	186	185	181	176	168	157	154
0.65	195	191	187	185	183	181	178	173	166	155	152
0.66	192	189	185	183	181	180	176	172	164	154	150
0.67	190	186	183	181	179	178	174	170	162	153	148
0.68	185	183	180	178	176	175	172	167	160	150	144
0.69	183	179	177	175	173	172	169	164	157	147	141
0.70	179	176	173	172	170	169	166	161	154	145	137
0.71	174	170	168	167	166	164	161	157	150	140	133
0.72	168	166	164	162	161	160	157	153	146	137	129
0.73	164	161	160	158	157	156	153	149	143	134	127
0.74	160	158	156	154	154	153	150	146	140	131	124
0.75	157	155	153	152	151	150	148	144	138	129	123
0.76	155	152	151	150	149	148	145	142	136	128	121
0.77	152	150	148	147	146	145	143	140	134	126	120
0.78	150	148	146	145	144	144	141	138	133	125	118
0.79	148	146	144	144	143	142	140	138	131	124	118
0.80	146	144	143	142	142	141	139	135	130	123	116
0.81	144	142	141	140	140	139	136	134	128	121	115
0.82	141	139	138	137	137	136	134	131	126	119	113
0.83	138	136	135	135	134	133	131	128	124	117	111
0.84	135	133	132	131	131	130	127	125	121	114	109
0.85	132	130	129	128	128	127	125	123	118	112	105
0.86	129	127	126	126	125	125	123	120	116	110	105
0.87	127	125	124	124	123	123	121	118	114	108	104
0.88	126	124	123	123	123	122	120	118	114	108	104
0.89	127	125	125	124	124	123	122	119	115	109	106

Table 21. Vertical profiles of spectral net flux $F_N = (F^{\downarrow} - F^{\uparrow}) \cdot 10^4$ $\frac{\text{watts}}{\text{cm}^2 \mu\text{m}}$
Model I

	P(mb)										
λ(μm)	0	100	200	300	400	500	600	700	800	900	1000
0.42	770	767	766	765	765	764	762	758	754	744	713
0.43	815	812	811	810	810	809	808	804	798	788	756
0.44	860	858	856	856	855	854	853	849	843	833	799
0.45	899	896	895	894	894	893	892	888	882	872	836
0.46	924	921	920	919	918	918	916	912	906	895	859
0.47	940	936	934	933	933	932	930	326	920	908	873
0.48	941	936	934	933	932	932	930	325	919	909	872
0.49	928	923	921	920	919	919	917	913	906	896	861
0.50	904	899	896	895	894	894	892	888	882	871	838
0.51	870	863	861	860	858	858	856	852	846	836	803
0.52	832	825	822	821	820	819	817	813	807	798	766
0.53	797	789	786	784	783	782	780	777	770	762	731
0.54	765	757	753	752	750	750	747	744	738	729	700
0.55	739	730	726	724	723	721	720	716	710	700	685
0.56	718	708	704	703	701	700	698	695	689	681	653
0.57	700	690	687	685	684	682	680	677	671	663	636
0.58	686	676	672	670	668	667	665	661	656	648	621
0.59	671	661	657	655	654	652	650	646	641	633	607
0.60	656	645	641	640	638	636	634	630	625	618	592
0.61	638	628	625	623	622	620	618	615	610	603	578
0.62	618	610	606	605	604	602	600	597	593	586	561
0.63	597	590	587	586	585	584	582	579	575	568	544
0.64	584	578	575	574	573	572	571	568	564	557	535
0.65	564	559	557	556	556	555	553	551	547	541	519
0.66	548	543	541	541	540	540	538	536	532	526	505
0.67	533	530	528	527	527	526	525	523	519	513	493
0.68	520	516	515	514	514	514	512	510	507	502	481
0.69	506	503	502	502	501	501	500	498	494	489	470
0.70	492	490	489	489	488	488	487	485	482	477	458
0.71	478	476	476	475	475	475	474	472	469	464	446
0.72	463	461	460	460	460	459	458	457	454	449	432
0.73	448	446	445	445	445	444	443	442	439	434	418
0.74	433	432	431	431	430	430	429	428	425	420	404
0.75	421	419	418	418	418	418	417	415	413	408	393
0.76	409	408	407	407	407	407	406	404	402	397	382
0.77	401	400	399	399	398	398	398	396	393	390	375
0.78	394	393	393	392	392	392	391	360	387	383	369
0.79	388	387	386	386	386	386	385	384	381	377	363
0.80	381	380	380	380	380	380	379	378	375	371	358
0.81	374	373	373	373	373	373	372	371	368	364	351
0.82	365	364	364	364	364	364	363	362	360	356	343
0.83	355	355	354	354	354	354	353	352	350	346	334
0.84	344	343	343	343	343	343	342	341	339	335	323
0.85	333	332	332	332	332	332	331	330	328	324	313
0.86	322	322	322	322	322	322	321	320	318	315	303
0.87	315	314	314	314	314	314	313	312	310	307	296
0.88	311	310	310	310	310	310	309	308	306	303	292
0.89	312	311	311	311	311	311	310	309	307	304	293

Table 22. Vertical profiles of spectral net flux $F_N = (F^{\downarrow} - F^{\uparrow}) \cdot 10^4$ $\frac{\text{watts}}{\text{cm}^2 \mu\text{m}}$
Model II

	P(mb)										
λ(μm)	0	100	200	300	400	500	600	700	800	900	1000
0.42	739	712	696	691	685	684	675	660	639	612	532
0.43	777	749	733	727	721	721	709	692	668	637	544
0.44	815	786	769	763	757	757	743	723	696	662	561
0.45	847	818	799	793	787	786	770	748	718	687	573
0.46	861	831	814	808	802	801	786	766	738	704	604
0.47	863	834	818	812	807	805	792	774	750	720	631
0.48	850	822	807	802	797	795	783	769	749	723	648
0.49	825	799	785	781	776	774	769	753	737	717	658
0.50	789	766	753	749	745	742	735	727	716	701	658
0.51	758	734	722	718	715	711	704	697	686	671	630
0.52	725	701	689	685	682	678	671	664	653	639	600
0.53	693	670	658	654	651	647	640	633	623	609	572
0.54	665	641	630	626	623	619	612	605	596	583	547
0.55	641	618	607	603	600	596	589	582	573	560	526
0.56	622	599	588	584	581	577	570	563	553	540	506
0.57	607	583	573	569	565	562	554	547	537	524	489
0.58	594	570	559	556	552	548	540	533	523	510	475
0.59	580	557	547	543	539	535	526	519	509	496	460
0.60	567	543	533	529	525	521	512	505	494	482	446
0.61	552	529	519	516	513	508	500	493	483	470	435
0.62	534	514	505	500	498	494	486	479	470	456	422
0.63	518	499	491	488	485	482	474	468	458	445	411
0.64	505	488	480	477	474	471	464	458	448	436	403
0.65	488	472	465	462	460	467	450	444	435	423	391
0.66	479	464	457	455	453	450	444	439	430	420	390
0.67	472	458	452	450	448	446	440	436	428	418	390
0.68	465	453	447	445	443	441	437	432	426	417	390
0.69	458	470	442	440	438	436	433	429	423	415	391
0.70	452	441	437	435	433	432	429	426	421	414	391
0.71	441	431	426	425	423	422	419	416	412	405	383
0.72	428	419	415	413	412	410	408	405	400	394	374
0.73	416	407	403	402	400	399	396	394	390	384	364
0.74	404	396	392	390	389	388	386	383	380	375	355
0.75	394	386	382	381	380	379	377	374	371	366	347
0.76	385	377	373	372	371	370	368	366	363	358	339
0.77	378	370	366	365	364	363	361	359	356	351	333
0.78	372	364	361	360	359	358	356	354	351	346	329
0.79	367	360	356	355	354	353	351	350	346	342	324
0.80	361	354	351	350	349	348	347	345	342	337	320
0.81	355	348	345	344	343	342	341	340	336	332	315
0.82	347	340	338	337	336	335	334	332	329	325	308
0.83	338	332	329	328	327	326	325	323	320	316	301
0.84	327	321	319	318	317	316	135	313	311	307	292
0.85	317	312	309	308	307	307	305	304	301	298	283
0.86	308	302	300	299	298	297	296	295	292	289	274
0.87	301	295	293	292	291	291	290	288	286	282	268
0.88	297	292	289	288	288	287	286	285	282	278	265
0.89	298	293	291	290	289	288	287	286	284	280	266

Table 23. Vertical profiles of spectral net flux $F_N=(F^{\downarrow} - F^{\uparrow}) \cdot 10^4$ $\frac{\text{watts}}{\text{cm}^2\mu\text{m}}$
Model III

	P(mb)										
λ(μm)	0	100	200	300	400	500	600	700	800	900	1000
0.42	836	828	820	817	815	815	801	784	760	727	636
0.43	892	883	876	872	868	869	853	833	804	767	668
0.44	950	940	932	927	924	924	906	832	850	807	700
0.45	1001	990	980	976	972	972	950	925	889	841	726
0.46	1014	1004	995	991	987	987	968	946	913	871	764
0.47	1014	1004	997	993	990	990	974	955	927	891	796
0.48	995	987	982	987	976	976	963	948	926	896	815
0.49	963	956	951	949	947	947	939	923	911	889	325
0.50	918	911	908	906	905	904	901	894	884	869	324
0.51	883	876	872	871	869	868	864	858	848	834	790
0.52	845	837	833	832	830	829	825	819	810	796	754
0.53	808	800	796	794	793	792	788	782	773	760	720
0.54	776	767	763	761	760	759	755	749	740	728	689
0.55	749	739	736	734	732	731	727	721	712	701	664
0.56	730	720	716	713	712	711	706	700	692	679	642
0.57	714	703	699	697	695	694	689	683	674	661	623
0.58	701	690	685	683	681	680	675	668	659	646	607
0.59	688	677	672	670	668	666	661	654	644	631	592
0.60	674	662	656	655	653	652	646	639	629	615	575
0.61	657	646	642	640	638	636	631	624	614	600	561
0.62	637	627	624	621	620	618	613	606	596	583	545
0.63	616	608	604	602	601	600	595	583	578	565	528
0.64	602	595	592	591	589	583	583	577	567	555	518
0.65	583	577	574	573	571	571	566	559	550	538	503
0.66	563	558	555	554	553	552	548	543	535	523	491
0.67	546	541	539	539	537	537	537	533	528	521	482
0.68	529	525	524	523	522	522	518	515	509	500	473
0.69	513	510	506	508	507	507	504	500	495	488	464
0.70	496	494	493	492	492	492	490	487	482	476	455
0.71	482	480	479	478	478	477	476	473	469	453	443
0.72	466	464	463	462	462	462	460	453	454	449	429
0.73	450	448	447	447	447	446	445	443	439	434	419
0.74	435	433	432	432	432	432	430	428	425	420	403
0.75	422	420	419	419	419	419	418	416	413	408	392
0.76	410	409	406	408	408	408	406	405	402	398	381
0.77	402	400	400	400	399	399	398	396	393	389	374
0.78	395	394	393	393	333	393	392	390	387	383	368
0.79	389	388	387	387	387	387	386	384	381	377	362
0.80	382	381	381	380	380	380	380	378	375	371	357
0.81	375	374	374	374	374	374	373	371	369	365	350
0.82	366	365	365	365	365	365	364	362	360	356	342
0.83	356	355	355	355	355	355	353	352	350	346	333
0.84	344	344	343	342	342	342	342	341	338	335	322
0.85	333	333	332	332	332	332	332	330	326	325	312
0.86	323	322	322	322	322	322	321	320	318	314	302
0.87	315	315	314	314	314	314	314	312	310	307	295
0.88	311	311	310	310	310	310	309	308	306	303	292
0.89	312	312	311	311	311	311	310	309	307	304	292

Table 24. Vertical profiles of spectral flux divergence for the three calculational models $\Delta F_{N,\lambda} = [F_{N,\lambda}(P_1) - F_{N,\lambda}(P_2)] \cdot 10^4 \frac{\text{watts}}{\text{cm}^2 \mu\text{m}}$

	ΔP(mb)											
	0-500			500-900			900-1000			0-1000		
λ(μm)	I	II	III	I	II	III	I	II	III	I	II	III
0.42	6	55	21	20	62	88	31	80	91	57	207	200
0.43	6	56	23	21	84	102	32	93	99	59	233	224
0.44	6	58	26	21	95	117	34	101	107	61	254	250
0.45	6	61	29	21	99	131	36	114	115	63	274	275
0.46	6	60	27	23	97	116	36	100	107	65	257	250
0.47	8	58	27	24	85	99	35	89	95	67	232	218
0.48	9	55	20	23	72	80	37	75	81	69	202	181
0.49	9	51	16	23	57	58	35	59	64	67	167	138
0.50	9	47	14	23	41	35	33	43	45	66	131	94
0.51	12	47	15	22	40	34	33	41	44	67	128	93
0.52	13	47	16	21	39	33	32	39	42	66	126	91
0.53	15	46	16	20	38	32	31	37	40	66	121	88
0.54	15	46	17	21	36	31	29	36	39	65	118	87
0.55	18	45	18	20	36	30	27	34	37	65	115	85
0.56	18	45	19	19	37	32	28	35	37	65	116	88
0.57	18	45	20	19	38	33	27	35	38	64	118	91
0.58	19	46	21	19	38	34	27	36	39	65	119	94
0.59	19	45	22	19	39	35	26	36	39	64	120	96
0.60	20	46	22	18	39	37	26	35	40	64	121	99
0.61	18	44	22	17	38	36	25	34	39	60	120	96
0.62	16	40	19	16	38	35	25	34	38	57	112	92
0.63	13	36	16	16	37	35	24	33	37	53	109	88
0.64	12	34	14	15	35	33	22	32	37	49	102	84
0.65	9	21	12	14	44	33	22	30	35	45	97	80
0.66	8	29	11	14	30	29	21	28	32	43	89	72
0.67	7	26	9	13	28	16	20	27	39	40	82	64
0.68	6	24	7	12	24	22	21	24	27	39	75	66
0.69	5	22	6	12	21	19	19	23	24	36	67	49
0.70	4	20	4	11	18	16	19	22	21	34	61	41
0.71	3	20	5	11	17	14	18	22	20	32	59	39
0.72	4	18	4	10	16	15	17	20	20	31	54	39
0.73	4	18	4	10	15	12	16	20	15	30	53	31
0.74	4	16	3	10	13	12	16	20	17	30	49	32
0.75	3	15	3	10	13	11	15	19	16	28	47	30
0.76	2	15	2	10	12	10	15	19	17	27	46	29
0.77	3	15	3	8	12	10	15	18	15	26	45	28
0.78	2	14	2	9	12	10	14	17	15	25	43	27
0.79	2	14	2	9	11	10	14	18	15	25	43	27
0.80	1	13	2	9	11	9	13	17	14	23	41	25
0.81	1	13	1	9	10	9	13	17	15	22	40	25
0.82	1	12	1	8	10	9	13	17	14	21	39	24
0.83	1	12	1	8	10	9	12	15	13	21	37	23
0.84	1	11	1	8	9	7	12	15	13	20	35	21
0.85	1	10	1	8	9	7	11	15	13	20	34	21
0.86	0	11	1	7	8	8	12	15	12	19	34	21
0.87	1	10	1	7	9	7	11	14	12	19	33	20
0.88	1	10	1	7	9	7	11	13	11	19	32	19
0.89	1	10	1	7	8	7	11	14	12	19	32	20

Table 25. Vertical profile of spectral albedo. $A_\lambda \cdot 10^3$
Model I

	P(mb)										
λ(μm)	0	100	200	300	400	500	600	700	800	900	1000
0.42	295	284	287	281	273	253	215	191	167	136	91
0.43	290	281	281	275	268	250	215	198	172	142	104
0.44	285	275	275	269	263	246	216	200	177	160	115
0.45	279	270	266	260	254	242	217	202	180	155	124
0.46	276	268	263	257	251	241	219	204	187	161	137
0.47	274	265	259	253	246	235	219	207	187	165	138
0.48	270	262	256	250	244	237	221	208	190	168	144
0.49	266	260	253	247	240	235	220	209	193	172	149
0.50	263	257	250	244	240	235	222	212	198	176	154
0.51	263	257	250	245	240	236	225	215	201	181	161
0.52	263	258	251	247	241	238	228	218	205	187	169
0.53	262	258	251	247	242	240	231	222	209	191	175
0.54	263	259	252	248	244	241	234	226	220	197	182
0.55	263	259	253	250	245	243	237	230	218	202	184
0.56	264	261	255	252	248	247	241	233	222	208	194
0.57	265	262	258	254	251	249	244	237	226	212	201
0.58	265	263	259	256	253	252	245	239	219	216	205
0.59	266	264	260	258	255	254	249	243	234	220	210
0.60	267	266	262	259	257	255	252	246	237	224	215
0.61	270	268	265	262	260	258	255	250	241	228	221
0.62	272	271	267	265	263	262	259	253	245	232	226
0.63	276	275	272	270	267	265	263	258	250	238	234
0.64	271	270	267	265	262	261	258	253	244	233	227
0.65	273	271	268	267	265	291	260	256	247	236	232
0.66	275	272	270	269	267	265	262	257	249	237	235
0.67	274	273	269	267	268	264	261	257	250	238	234
0.68	273	270	268	267	265	265	261	256	249	237	234
0.69	272	269	266	266	263	259	255	246	237	237	232
0.70	270	268	265	264	263	261	258	253	246	235	231
0.71	270	267	265	263	262	261	257	253	244	234	231
0.72	269	266	264	264	263	262	258	253	245	235	231
0.73	271	268	266	265	264	262	260	254	248	237	233
0.74	272	270	268	265	264	263	261	257	250	239	236
0.75	274	271	268	269	266	267	263	258	251	241	238
0.76	276	274	271	272	271	269	266	262	257	246	242
0.77	276	274	271	273	271	269	265	262	257	246	242
0.78	277	274	272	270	271	270	265	262	254	246	244
0.79	277	275	274	273	271	270	263	264	257	247	245
0.80	278	278	274	275	273	273	268	264	258	248	244
0.81	279	277	275	274	274	272	270	265	259	251	246
0.82	280	277	275	274	274	273	271	267	261	250	247
0.83	281	279	277	277	276	274	272	268	261	252	249
0.84	281	281	279	277	278	276	273	269	263	253	252
0.85	283	282	279	279	270	278	275	273	266	256	254
0.86	285	284	282	283	281	279	274	269	258	258	257
0.87	287	286	284	283	283	283	280	276	272	262	260
0.88	288	287	285	286	284	284	281	276	271	262	262
0.89	289	288	286	287	285	285	282	279	274	263	263

Table 26. Vertical profile of spectral albedo. $A_\lambda \cdot 10^3$
Model II.

	P(mb)										
λ(μm)	0	100	200	300	400	500	600	700	800	900	1000
0.42	323	310	286	274	266	251	222	199	165	124	9
0.43	323	310	286	278	268	257	226	203	171	130	106
0.44	323	309	291	274	270	256	226	207	177	142	117
0.45	320	308	290	281	268	254	232	212	182	140	126
0.46	327	314	298	289	279	268	244	224	194	151	134
0.47	334	320	306	298	288	266	230	215	186	163	140
0.48	341	324	315	307	298	291	280	249	219	177	146
0.49	348	336	325	317	309	302	277	262	232	189	152
0.50	357	345	335	328	320	317	299	280	249	202	157
0.51	358	346	336	330	322	319	302	281	254	210	164
0.52	358	347	338	336	324	323	306	288	232	215	171
0.53	359	345	339	332	326	324	310	291	263	220	177
0.54	359	349	341	334	328	326	309	296	267	226	186
0.55	360	350	341	336	331	330	314	300	270	231	192
0.56	363	352	344	338	333	332	321	304	277	235	197
0.57	364	357	347	341	336	336	321	307	281	240	204
0.58	364	357	348	343	338	338	326	310	283	244	210
0.59	365	359	350	346	341	340	329	320	287	247	215
0.60	367	360	351	347	342	343	328	316	291	251	218
0.61	369	362	354	350	346	346	331	318	293	253	225
0.62	371	365	357	352	348	348	332	321	311	258	229
0.63	372	365	357	352	348	348	337	322	297	260	233
0.64	370	362	354	350	346	344	329	318	292	255	232
0.65	372	363	356	352	348	347	334	319	296	259	236
0.66	366	357	349	344	341	341	327	316	293	257	238
0.67	358	348	342	336	334	332	319	309	289	255	238
0.68	350	339	331	328	324	323	311	301	282	254	236
0.69	341	326	323	323	315	314	306	295	276	250	234
0.70	331	318	311	309	306	304	294	288	272	247	233
0.71	327	315	308	305	301	301	292	283	268	245	232
0.72	324	313	306	302	299	297	291	281	266	246	233
0.73	321	309	303	301	298	296	289	284	266	247	235
0.74	320	309	303	298	297	294	287	279	266	246	238
0.75	318	307	300	297	295	292	287	278	266	248	238
0.76	318	306	299	298	294	293	288	280	268	251	243
0.77	319	305	300	298	294	293	285	280	269	251	244
0.78	317	304	299	294	293	292	287	280	268	250	245
0.79	316	303	299	295	293	292	286	279	267	253	245
0.80	318	303	298	295	295	290	286	279	269	254	248
0.81	315	304	298	294	292	291	286	280	269	253	247
0.82	315	302	297	294	293	291	286	279	268	254	250
0.83	315	303	298	296	292	290	285	280	271	256	251
0.84	317	304	299	296	294	293	287	282	272	256	253
0.85	318	305	299	296	293	292	288	283	272	258	257
0.86	318	306	300	293	297	289	291	283	274	263	259
0.87	319	306	302	299	296	295	292	288	278	265	263
0.88	320	307	301	300	297	295	292	288	278	265	263
0.89	321	308	302	301	298	296	292	288	279	267	273

Table 27. Vertical profile of spectral albedo. $A_\lambda \cdot 10^3$ Model III

	P(mb)										
λ(μm)	0	100	200	300	400	500	600	700	800	900	1000
0.42	234	223	205	193	181	169	148	134	117	100	94
0.43	222	211	194	188	171	159	144	131	117	102	104
0.44	210	200	184	174	164	155	140	130	118	107	115
0.45	197	192	174	165	155	146	136	128	119	110	123
0.46	206	199	185	176	168	159	150	141	133	121	132
0.47	216	210	197	189	181	173	164	154	144	133	138
0.48	238	220	209	202	195	188	177	169	158	145	144
0.49	237	232	223	216	210	203	193	183	171	156	149
0.50	253	246	238	232	227	222	210	200	187	170	155
0.51	252	246	241	236	229	225	214	205	191	175	161
0.52	253	247	239	235	230	226	217	208	195	180	168
0.53	253	248	240	236	231	228	220	212	200	185	175
0.54	252	248	242	238	234	230	223	215	204	191	183
0.55	253	249	243	239	235	233	227	220	210	197	189
0.56	252	249	242	240	236	234	228	222	212	200	196
0.57	251	248	243	239	237	235	230	223	216	204	202
0.58	250	247	242	240	237	235	231	225	218	204	206
0.59	248	247	242	239	236	235	232	226	220	210	211
0.60	246	246	241	237	237	236	232	228	222	212	216
0.61	245	247	243	241	239	238	235	231	225	216	221
0.62	251	249	246	244	242	241	238	234	229	220	226
0.63	254	253	249	247	245	244	242	239	233	225	235
0.64	248	247	243	242	240	239	236	233	228	220	230
0.65	248	248	245	244	242	241	239	236	231	223	229
0.66	254	253	249	247	246	246	242	240	234	227	235
0.67	258	255	253	251	250	250	245	243	236	230	240
0.68	260	258	255	253	252	252	248	244	239	231	238
0.69	263	259	258	256	254	255	251	246	240	231	239
0.70	265	262	259	259	256	256	253	248	241	233	238
0.71	265	261	259	258	258	255	251	249	242	232	230
0.72	264	263	261	259	258	256	254	250	243	234	230
0.73	267	263	263	261	259	258	255	251	245	235	234
0.74	268	267	265	262	263	261	258	254	247	237	235
0.75	271	269	267	265	264	264	261	257	250	240	239
0.76	273	271	270	268	267	266	262	259	252	243	240
0.77	274	272	270	268	267	266	263	260	253	244	242
0.78	275	273	270	269	267	268	264	261	255	246	242
0.79	275	273	270	271	269	268	266	262	255	247	245
0.80	276	274	272	271	272	270	268	263	257	248	245
0.81	277	275	273	272	272	271	266	265	257	248	246
0.82	278	275	274	272	273	272	269	265	259	250	248
0.83	279	276	275	276	274	272	270	266	261	252	250
0.84	281	278	277	276	276	274	272	268	263	253	252
0.85	283	280	279	277	278	276	273	271	264	256	255
0.86	285	282	280	281	279	279	277	272	267	258	257
0.87	287	284	282	283	280	281	278	273	268	259	260
0.88	288	285	283	284	284	282	279	276	271	262	263
0.89	289	286	286	285	285	283	282	278	272	263	265

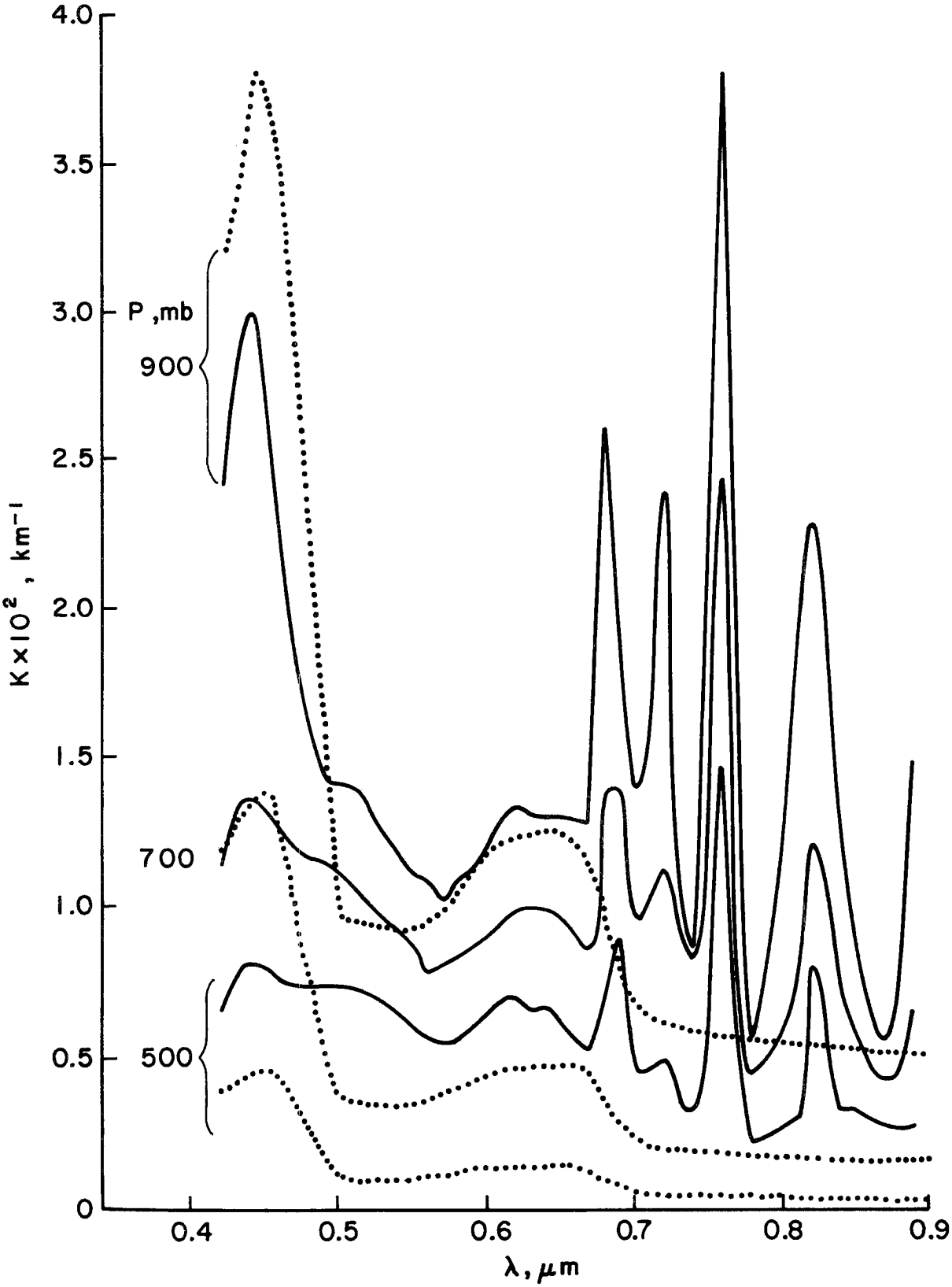

Figure 3. Spectral absorption coefficient for 3 levels in the atmosphere. _____ experiment .... Models II and III

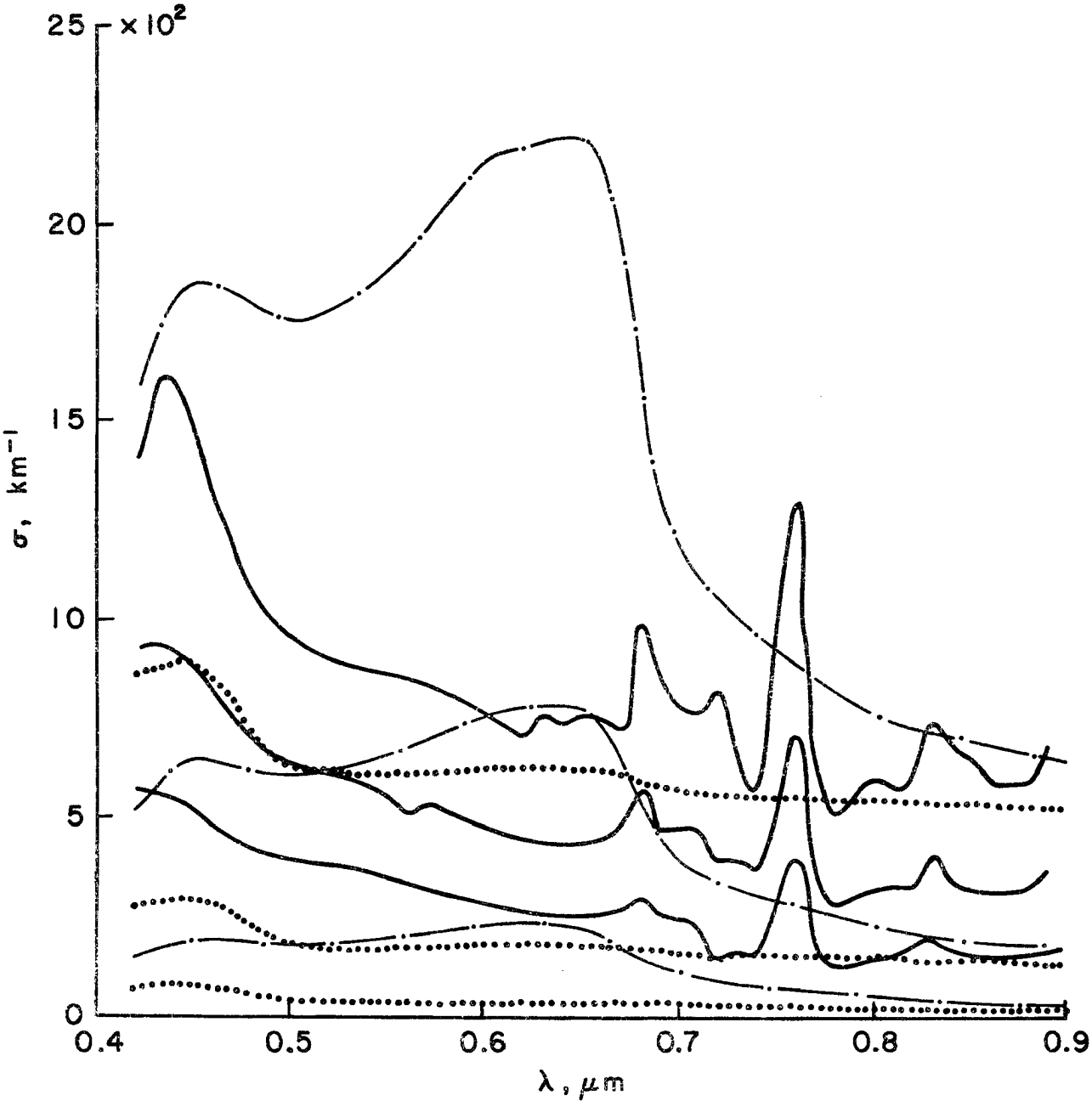

Figure 4. Spectral extinction coefficient for 3 levels in the atmosphere.
_____ experiment -.- Model II ... Model III

The short analysis of the calculations made for the different aerosol models gives an estimation of the impact of aerosol parameters upon the radiation field. A more detailed analysis will permit one to judge the applicability of the models to properly describe the radiation characteristics in the real atmosphere. In addition, results from such analysis may be used to help determine how representative are experimental data on aerosol composition and concentration.

After the preliminary analysis mentioned in the previous section, the following aerosol models were chosen for a more detailed treatment:

(a) Model I - the "mean" aerosol, whose optical characteristics are given in Tables 10 and 11. This model is predominantly characterized by scattering; absorption is small.

(b) Model II - the "mean" aerosol plus absorption and scattering due to hematite in the wave length range 0.4-0.5μm. Hematite was detected in the form of separate small particles with a narrow size distribution range centered about 0.1μm. Therefore, it appears reasonable to include hematite as an additional scattering and absorption aerosol to the "mean" aerosol. Due to the small size of the hematite particles, the hematite phase function was assumed to be approximated by Rayleigh phase function.

(c) Model III - the "mean" aerosol plus absorbing hematite alone. This model is intermediate between the first two models. It suggests that hematite is included in the composition of aerosol particles. Scattering properties of this model correspond to the "mean" aerosol ensemble of Model I. Such representation of the absorption coefficient is based upon the

(c) fact that ferric compounds generally exist as one of the components of aerosol particles. The concentration profile of hematite particles in Table 14 was estimated from data on the mean mass hematite concentrations in aerosol samples.

Results of calculations of atmospheric radiation corresponding to the Models I, II, and III along with experimental data are given in Figures 5-9. Comparison between measured and calculated values of downward fluxes (Figure 5) shows the best fit for Models II and III in which hematite is included. Once again the poorest agreement is for Model I which is connected to the fact that aerosol particles in this model have low absorption.

In the case of upward fluxes (Figure 6), the best fit of calculated and measured values corresponds to Model III. Again, the worst agreement is for Model I. Model II overestimates the role of scattered radiation as compared to absorbed.

Comparison between calculated and measured values of the spectral net flux for two levels (P=0 and 1000 mb) shows (Figure 7) the best fit for Model III. Model I underestimates absorbing properties of the aerosol. Calculations using Model II yield even smaller values of net flux at the P=0 mb level since the upward flux is overestimated. Therefore, there is an overestimation of scattered radiation as compared to absorbed radiation. It should be recalled that the highest altitude at which measurements were taken is approximately 400 mb so that extrapolations to 0 mb may be in error. Likewise the lowest altitude at which measurements were taken is approximately 975 mb so that extrapolations down to the 1000 mb level through a dense aerosol layer may also be in error.

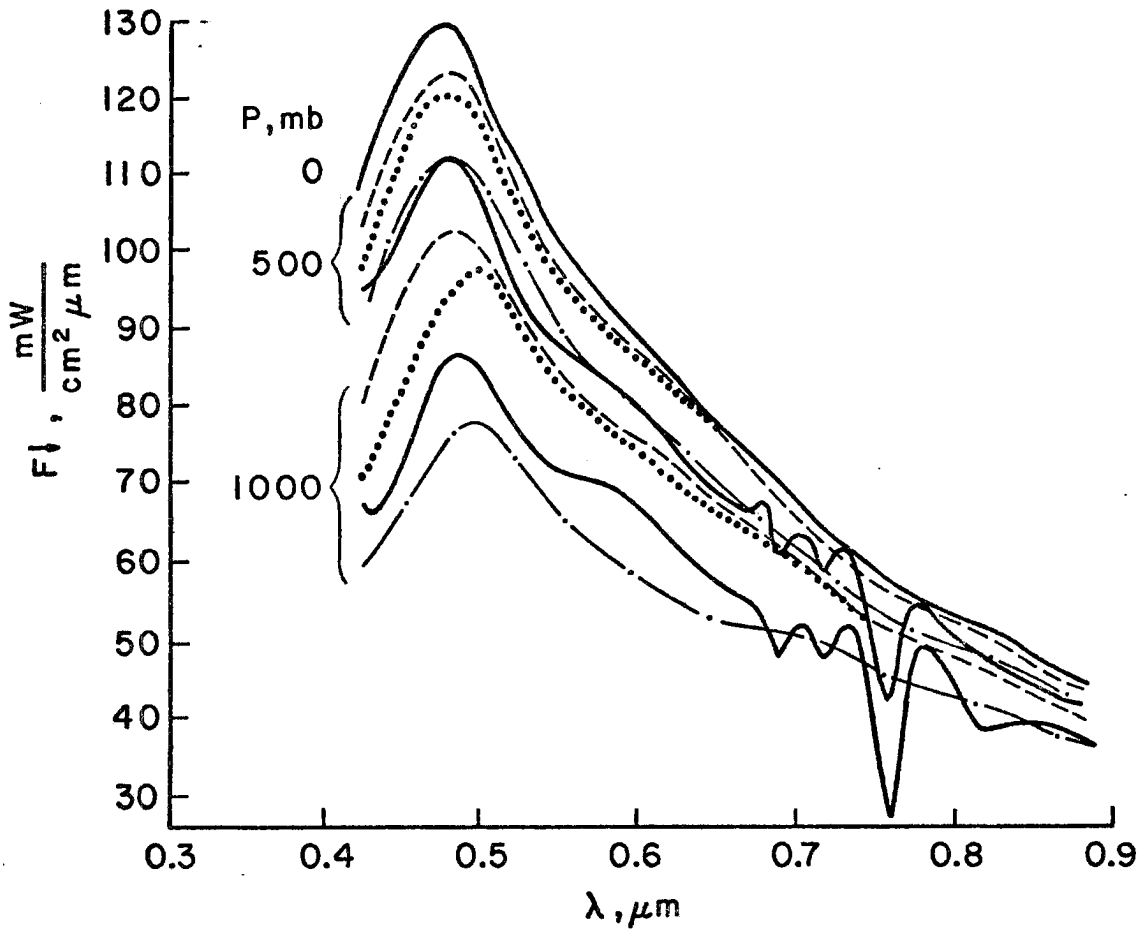

Figure 5. Spectral distribution of downward radiation flux for 3 levels in the atmosphere.
_____ experiment --- Model I -.- Model II ... Model III

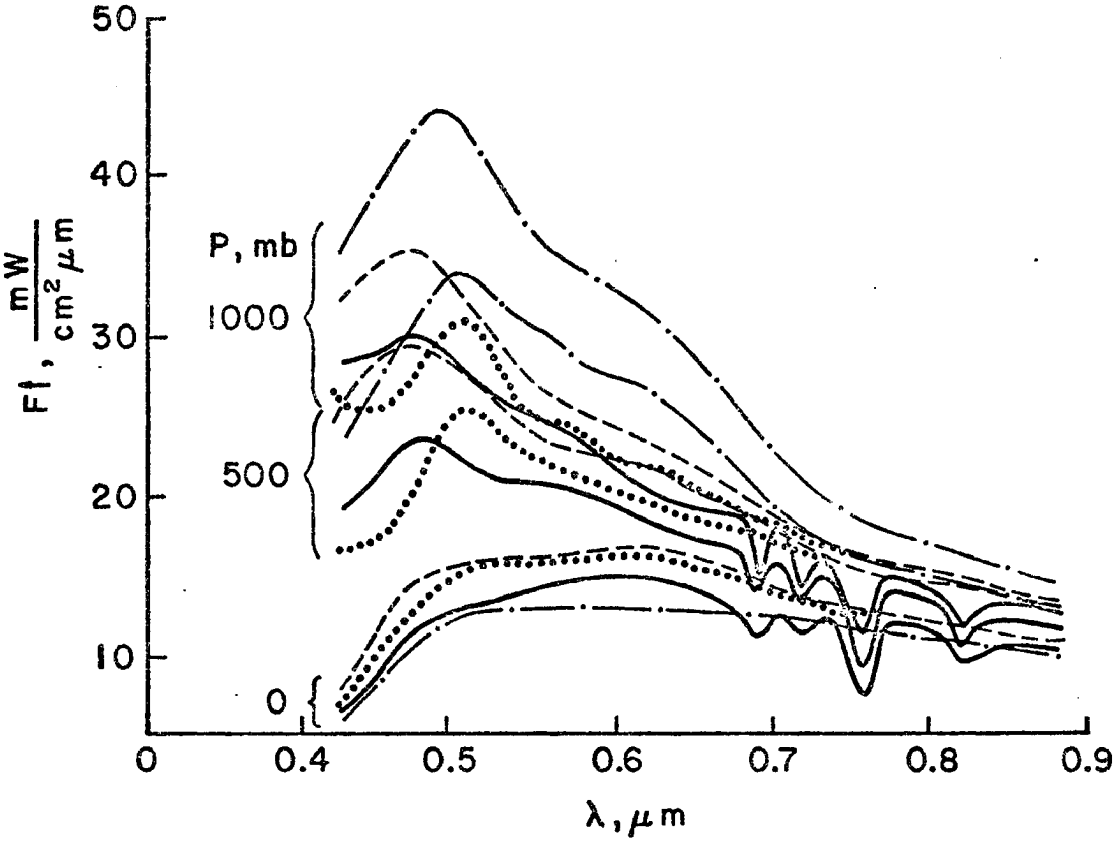

Figure 6. Spectral distribution of upward radiation flux for 3 levels in the atmosphere.
_____ experiment --- Model I -.- Model II ... Model III

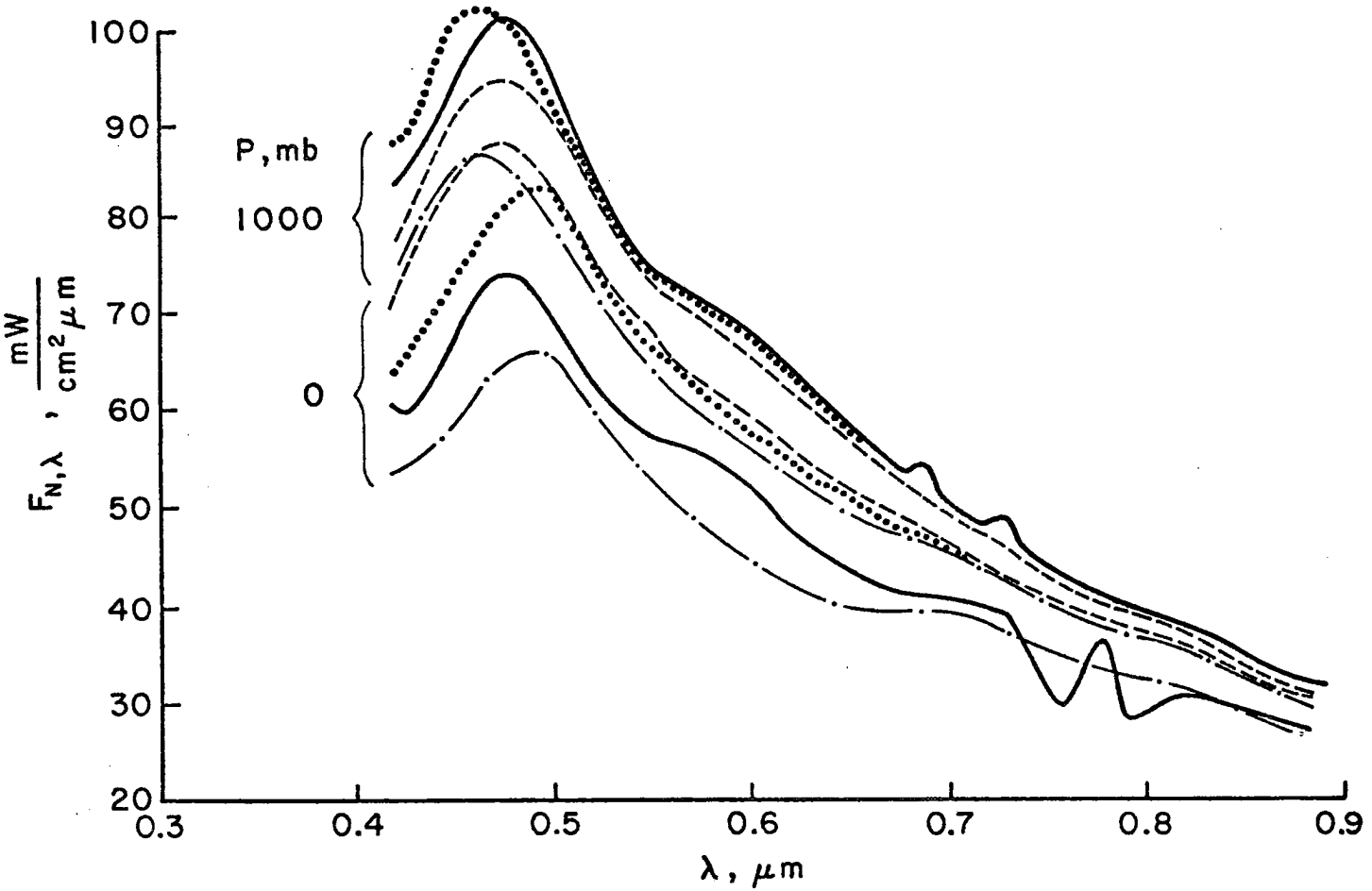

Figure 7. Spectral distribution of radiation balance (net flux) for 2 layers in the atmosphere. _____ experiment --- Model I -.- Model II ... Model III

The neglect of absorbing hematite properties, particularly in the spectral region 0.4-0.5μm, is most pronounced in Figure 8 which provides values of spectral radiative flux divergences between P=0 and P=1000 mb. As expected Model I gives the poorest agreement between measured and calculated values. Addition of hematite particles provides reasonable agreement in the hematite absorbing region. However, there is a systematic underestimation of the calculated values as compared to the measured values throughout the entire spectral region. Model II, which includes hematite scattering, provides better results than does Model III. Therefore, we conclude that increased scattering as well as increased absorption is necessary to obtain a "best fit" for the entire spectral range. It would appear either that particle concentrations have been underestimated or that "mean" aerosol scattering and absorption coefficients have been underestimated. In addition, there may also be other absorbing particles present in the atmosphere which were not considered in these calculations.

Comparison between calculated and measured values of spectral albedo in Figure 9 also shows the best agreement for Model III. Discrepancies between the data in the wavelength region 0.65-0.90μm are largely caused by the neglect of molecular absorption by oxygen and water vapor.

One may conclude that the most probable model is Model III, but with increased aerosol concentration. A model intermediate between Models II and III would appear to describe most correctly the real aerosol at the experimental site. A definitive answer to the question as to how hematite should be considered in the atmospheric aerosol can apparently be obtained from a specially devised experiment.

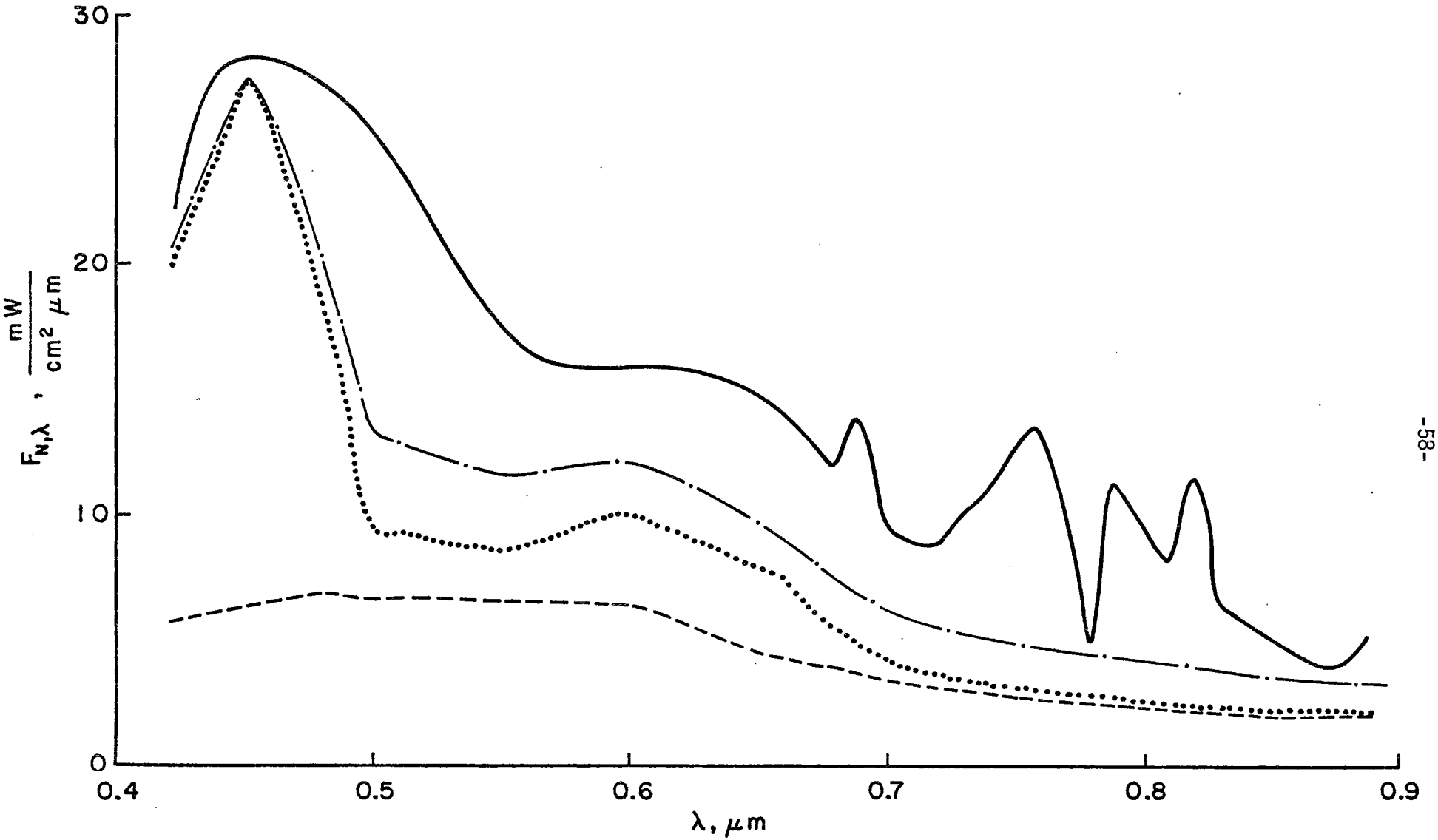

Figure 8. Spectral shortwave radiation heat balance (flux divergence) for the entire atmosphere.
_____ experiment --- Model I -.- Model II ... Model III

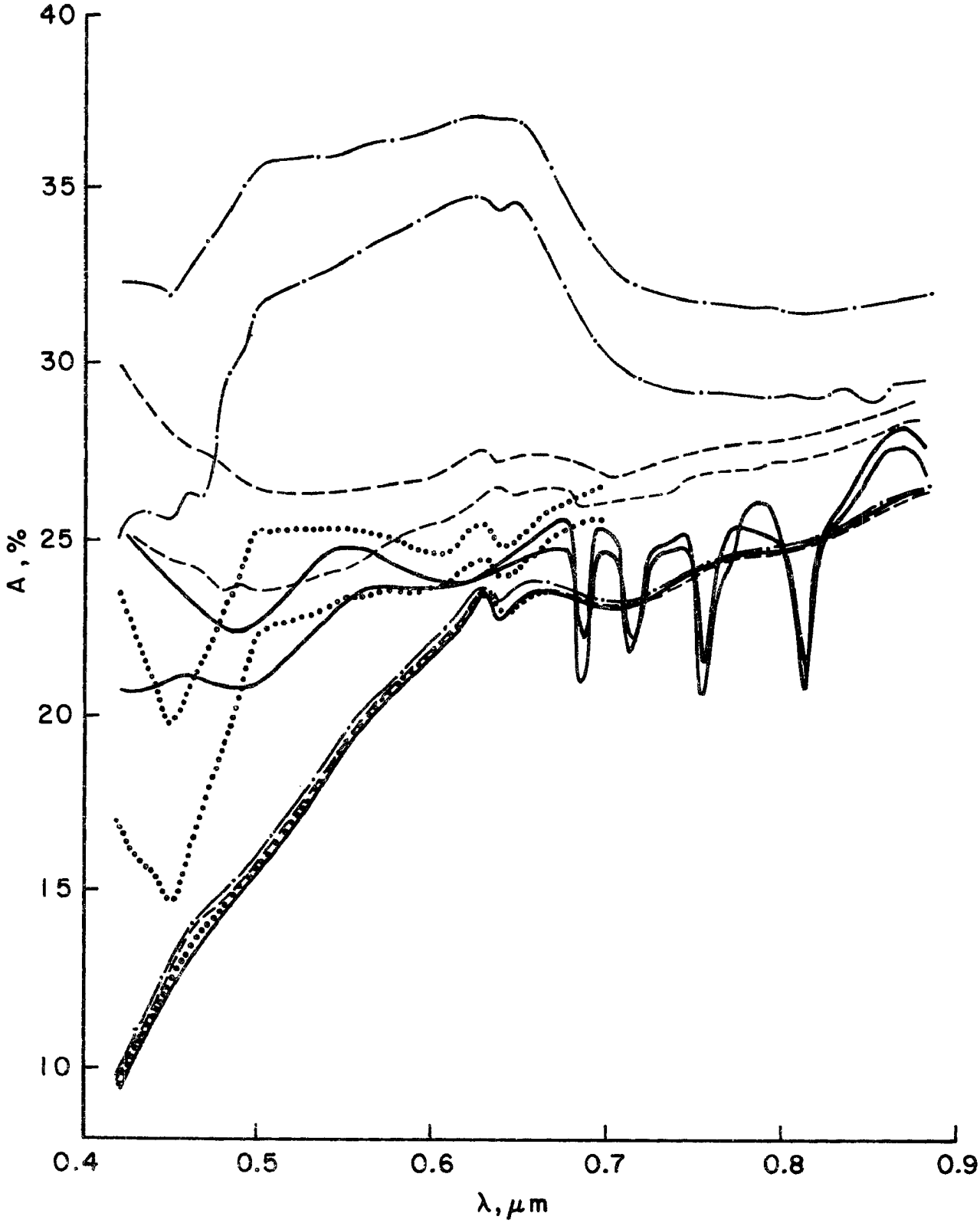

Figure 9. Spectral albedo for 3 levels in the atmosphere.
_____ experiment --- Model I -.- Model II ... Model III

6. Sensitivity Studies

A "best fit" between observations and calculations is difficult to obtain simultaneously for all spectral regions. Therefore, further studies have been made to test the sensitivity of calculations to small variations in input parameters. Model III was adopted in which hematite absorption was included without hematite scattering. Table 28 shows concentrations of aerosol and hematite for each of the ten vertical layers used in the sensitivity studies. Data given in the previous sections have been interpolated, extrapolated, and smoothed. In the sensitivity studies, calculations were performed only at selected wavelengths and only at those heights where measurements were taken.

Table 28. Aerosol and hematite concentrations (particles/cm^3) and layer thicknesses (m) for ten vertical layers: the left column corresponds to the layer closest to the surface.

Thickness (m)	200	150	525	1000	1050	1175	1375	2925	7850	13750
Aerosol Concentration	160	42	30	17	8	4	2	1	0.25	0.03
Hematite Concentration	1000	900	700	550	350	200	150	20	2	1

Applying the model adopted above, intercomparisons are shown in Table 29 at heights of 8400, 2830, and 300 m for which actual measurements were made. As can be seen, reasonable agreement exists for fluxes at λ=0.42 μm, even though the flux divergence disagrees by a factor of 2. At other wavelengths, disagreements between observations and calculations of flux divergences may reach a factor of 4. Therefore, the flux divergence and atmospheric heating rates are extremely sensitive to small variations in

Table 29. Intercomparisons between measured and calculated fluxes at selected wavelengths and heights.

		Measured			Model (Table 28)			Neglect of Size Distribution Variation		
λ(μm)	H(m)	$F^{\uparrow}$	$F^{\downarrow}$	F_N	$F^{\uparrow}$	$F^{\downarrow}$	F_N	$F^{\uparrow}$	$F^{\downarrow}$	F_N
.42	8400	234	1070	836	256	1042	786	253	1046	793
	2830	162	880	718	151	905	754	149	913	765
	300	92	700	608	80	742	662	82	757	676
.47	8400	258	1220	972	288	1246	957	282	1248	967
	2830	201	1030	829	205	1128	923	202	1138	936
	300	139	890	751	140	961	821	142	980	838
.52	8400	215	980	765	274	1092	819	267	1094	827
	2830	179	840	661	225	1029	804	223	1038	815
	300	134	750	616	170	932	762	173	950	777
.57	8400	206	910	704	236	921	685	231	923	692
	2830	183	770	587	205	875	670	204	883	679
	300	149	720	571	168	799	632	170	814	644
.62	8400	184	790	606	217	826	609	212	827	615
	2830	166	680	514	194	788	594	193	795	602
	300	148	630	482	166	720	555	168	733	565
.67	8400	175	710	535	192	722	529	189	723	534
	2830	159	610	451	175	694	519	174	700	526
	300	138	590	452	152	642	489	155	653	498
.72	8400	134	600	466	169	626	457	165	627	411
	2830	125	560	435	155	606	451	154	611	457
	300	107	480	373	135	568	433	137	577	440
.77	8400	125	530	405	152	548	396	150	549	399
	2830	127	490	363	142	533	391	141	557	396
	300	113	440	327	125	501	376	127	509	383
.82	8400	104	490	384	141	503	361	139	504	365
	2830	97	420	323	132	490	358	132	494	362
	300	93	390	297	117	462	344	119	469	350
.87	8400	121	430	309	127	439	312	125	439	314
	2830	112	400	288	120	428	308	119	431	312
	300	101	390	289	107	405	297	109	411	302

fluxes. A discussion of possible errors and recommendations will follow later.

Surface albedos were obtained from extrapolations of the observations through a thick dust layer of 300 m. Therefore an albedo sensitivity study was performed. Results are shown in Table 30 with albedos scaled as indicated. The upward fluxes are most strongly affected by albedo variations. With increasing albedo, the flux divergence increases since there is additional radiation available to be absorbed. However, differences resulting from albedo variations of 50% are negligible. Similar results hold for other wavelengths.

Aircraft observations took place over a span of 20 minutes at various altitudes. Therefore, the solar zenith angle of 54° adopted in this study represents a mean value. A sensitivity study of fluxes as a function of zenith angle is shown in Table 31. With increasing zenith angle, the flux divergence increases since the optical path length increases. Variations of zenith angles between 50° and 58° lead to corresponding variations in net flux divergence of less than 10%. Similar results hold for other wavelengths.

Ozone concentrations as a function of height were taken from a climatic model. Table 32 shows the influence of ozone concentrations arbitrarily increased by factors of 2, 3, and 4 upon the radiation field for three wavelengths. The flux divergence remains relatively insensitive to large ozone variations in the region λ = 0.40 μm to λ = 0.90 μm, even in the spectral region of maximum ozone absorption.

Variation of the size distribution with height was included in the original model. Aerosol absorption and extinction coefficients varied by 50% from the surface to a height of 500 mb. It had been expected

Table 30. Flux calculations at selected wavelengths and heights as a function of albedo, A_s.

		A_s ·0.50			A_s ·0.75			A_s ·1.0			A_s ·1.25			A_s ·1.50		
λ(μm)	H(m)	$F^{\uparrow}$	$F^{\downarrow}$	F_N	$F^{\uparrow}$	$F^{\downarrow}$	F_N	$F^{\uparrow}$	$F^{\downarrow}$	F_N	$F^{\uparrow}$	$F^{\downarrow}$	F_N	$F^{\uparrow}$	$F^{\downarrow}$	F_N
.42	8400	235	1039	505	245	1041	795	256	1042	786	267	1043	777	278	1045	767
	2830	129	902	773	140	904	764	151	905	754	162	907	744	174	908	735
	300	54	737	684	67	740	673	80	742	662	94	745	651	108	748	640
.47	8400	245	1243	997	267	1244	978	288	1246	957	310	1247	937	332	1249	917
	2830	161	1124	963	183	1126	943	205	1128	923	228	1131	902	251	1133	882
	300	86	953	866	113	957	844	140	961	821	167	965	799	194	970	775
.52	8400	216	1090	874	245	1091	846	274	1092	819	303	1093	790	333	1095	762
	2830	164	1024	859	194	1026	832	225	1029	804	256	1031	775	287	1034	746
	300	101	922	821	135	927	792	170	932	762	205	938	732	241	943	702
.57	8400	177	920	743	206	921	714	236	921	685	267	922	655	297	923	625
	2830	143	871	729	174	873	699	205	875	670	237	877	640	270	879	610
	300	96	790	693	132	795	663	168	799	632	204	804	600	241	809	568

Table 31. Flux calculations at selected wavelengths and heights as a function of zenith angle, θ_o.

λ(μm)	H(m)	$\theta_o = 50°$			$\theta_o = 52°$			$\theta_o = 54°$			$\theta_o = 56°$			$\theta_o = 58°$		
		$F^{\uparrow}$	$F^{\downarrow}$	F_N	$F^{\uparrow}$	$F^{\downarrow}$	F_N	$F^{\uparrow}$	$F^{\downarrow}$	F_N	$F^{\uparrow}$	$F^{\downarrow}$	F_N	$F^{\uparrow}$	$F^{\downarrow}$	F_N
.42	8400	244	1047	803	250	1045	795	256	1042	786	262	1039	777	269	1036	766
	2830	147	919	772	149	913	764	151	905	754	154	897	743	156	888	732
	300	81	765	684	81	754	674	80	742	662	80	730	650	80	716	636
.47	8400	276	1250	974	282	1248	966	288	1246	957	295	1243	948	302	1240	937
	2830	200	1142	942	203	1135	933	205	1128	923	208	1120	912	211	1111	900
	300	141	986	845	140	974	834	140	961	821	139	947	808	139	931	793
.52	8400	263	1096	833	268	1094	826	274	1092	819	280	1090	810	287	1088	801
	2830	219	1038	819	222	1033	812	225	1029	804	228	1023	795	232	1017	785
	300	170	949	779	170	941	771	170	932	762	170	922	752	170	911	741
.57	8400	228	924	696	232	923	691	236	921	685	241	920	679	246	918	672
	2830	201	882	682	203	879	676	205	875	670	208	871	663	211	866	656
	300	168	813	645	168	807	639	168	799	632	167	791	624	167	782	615

Table 32. Flux calculations at selected wavelengths and heights with Ozone concentrations arbitrarily increased by factors of 2, 3, and 4.

λ(μm)	H(m)	Ozone ·2			Ozone ·3			Ozone ·4		
		$F^{\uparrow}$	$F^{\downarrow}$	F_N	$F^{\uparrow}$	$F^{\downarrow}$	F_N	$F^{\uparrow}$	$F^{\downarrow}$	F_N
.57	8400	230	910	680	224	899	675	218	888	670
	2830	200	862	661	196	849	653	191	836	645
	300	165	786	622	162	773	612	159	761	602
.62	8400	211	816	605	206	807	601	200	797	597
	2830	190	776	589	185	765	580	181	754	573
	300	163	709	547	160	698	538	157	687	530
.67	8400	190	718	528	188	714	526	186	710	525
	2830	173	689	516	171	685	513	170	680	511
	300	151	637	486	150	633	483	149	628	479

that this effect had a major impact upon the atmospheric radiation field. However, Table 29 shows that neglect of the size distribution variation with height produced insignificant variations in the radiative fluxes and flux divergences. It should be pointed out that the size distribution variation was linearly interpolated between the surface and 500 mb. Inspection of Table 10 shows that a linear interpolation of values between the 500 and 1000 mb levels is unjustified. Detailed Mie calculations at intermediate levels would undoubtedly provide larger attenuation parameters than given by the linearly interpolated values.

The impactor used in observations becomes saturated in highly turbid conditions. Therefore, a size distribution, particularly for small particles, and concentrations tend to be underestimated. Table 33 shows the impact of increasing aerosol concentrations by 50% and 100% while leaving the hematite concentration unchanged. With increasing aerosol concentrations, the total downward flux decreases, the upward diffuse flux increases, and the net flux divergence increases. However, in all regions the net flux divergence remains significantly smaller than the observed values. Table 33 also shows the effect of increasing the hematite concentration by 50% and 100% while leaving the aerosol concentration unchanged. With increasing hematite concentration (neglecting hematite scattering) the total downward flux and upward diffuse flux decrease, and the net flux divergence increases. Increased hematite absorption has an influence out to a wavelength of λ = .72 μm but has its maximum effect in the wavelength region below λ = .50 μm. While increasing the hematite concentration by 100% leads to reasonable results for wavelengths below λ = .50 μm, flux divergence values between λ = .52 and λ = .62 μm are not well approximated with this model.

Table 33. Flux calculations at selected wavelengths and heights for aerosol concentrations increased by 50% and 100% while leaving hematite concentrations unchanged, and hematite concentrations increased by 50% and 100% while leaving aerosol concentrations unchanged.

		Aerosol Concentration ·1.5			Aerosol Concentration ·2.0			Hematite Concentration ·1.5			Hematite Concentration ·2.0		
λ(μm)	H(m)	$F^{\uparrow}$	$F^{\downarrow}$	F_N	$F^{\uparrow}$	$F^{\downarrow}$	F_N	$F^{\uparrow}$	$F^{\downarrow}$	F_N	$F^{\uparrow}$	$F^{\downarrow}$	F_N
.42	8400	269	1037	768	281	1033	752	241	1039	798	229	1037	808
	2830	163	894	731	173	884	710	138	892	755	126	880	754
	300	83	706	623	85	672	587	72	707	636	64	674	610
.47	8400	292	1240	948	326	1239	913	272	1244	972	258	1242	985
	2830	203	1101	897	234	1101	867	190	1115	925	175	1102	926
	300	130	879	749	142	874	732	129	923	794	119	886	768
.52	8400	291	1090	799	311	1088	777	270	1092	822	268	1092	824
	2830	236	1013	778	251	1004	752	221	1026	805	218	1024	806
	300	168	884	716	169	850	681	168	926	758	165	919	754
.57	8400	248	919	671	265	917	652	233	921	688	229	921	692
	2830	212	862	650	224	854	629	201	873	672	197	871	673
	300	163	757	594	164	730	566	165	792	627	162	785	623
.62	8400	224	824	599	241	822	581	212	825	614	207	825	619
	2830	196	775	578	209	768	560	188	785	596	183	782	599
	300	159	680	521	160	659	499	162	711	550	158	702	544
.67	8400	199	720	521	212	718	506	189	722	533	186	721	536
	2830	177	683	506	186	677	491	171	692	521	168	690	522
	300	147	608	462	146	589	442	150	635	486	147	629	482
.72	8400	177	624	447	186	623	437	168	626	458	167	626	459
	2830	160	598	438	166	591	426	154	606	452	153	605	452
	300	132	542	410	130	521	391	134	566	432	134	565	431
.77	8400	160	547	387	167	546	379	152	548	396	152	548	396
	2830	146	526	380	150	520	370	141	532	391	141	532	391
	300	122	480	358	120	461	341	125	501	376	124	500	376
.82	8400	148	502	353	155	501	346	141	503	362	141	503	362
	2830	136	488	347	140	478	338	132	490	358	132	489	358
	300	115	443	328	112	425	313	117	461	344	117	461	344
.87	8400	133	438	305	138	437	299	127	439	312	127	439	312
	2830	123	423	300	125	418	292	119	428	308	119	428	309
	300	105	388	284	102	373	271	107	404	297	107	404	297

Hematite concentrations were calculated from measurements of the total Fe_2O_3 mass assuming a delta function size distribution. The hematite size distribution is extremely difficult to measure for these small particles, particularly in saturated impactor samples. Due to these difficulties, the present model assumed a delta function distribution with a radius of 0.10 μm. Tables 34 and 35 show the hematite absorption and extinction cross-sections (μm^2) as a function of particle radius and wavelength. It is seen that even small variations in the hematite particles radius lead to large variations in absorption and extinction parameters. Therefore, it is clear that the delta function size distribution approach used in the present study is inadequate.

It is a normal procedure to assume that all contributing particles share a similar size distribution function, even if variations in height are included. Nevertheless, indications are that it may be necessary to provide size distributions for the various components of aerosol, or for at least such optically active particles as hematite. Some of the difficulties in providing reasonable fits between observations and calculations can be traced to the improper size distribution assumed for hematite, particularly in the region from 0.50 to 0.70 μm.

Table 36 shows the impact of increasing both aerosol and hematite concentrations by 50% and 100%. In this case, increased net flux divergences result which indicates that increased scattering as well as absorption is necessary to provide a better fit with observations. Nevertheless, for wavelengths larger than 0.50 μm, the flux divergence remains underestimated in the calculations.

While chemical analysis is relatively accurate, there may be errors in the determination of the complex index of refraction. Furthermore,

Table 34. Hematite absorption cross-section (μm^2) as a function of particle radius and wavelength.

	Particle radius (μm)				
λ(μm)	0.08	0.09	0.10	0.11	0.12
0.30	.00476	.01197	.00760	.01028	.01671
0.40	.01182	.04410	.02452	.04162	.05690
0.45	.00666	.00828	.03880	.01872	.02398
0.50	.00866	.00344	.00438	.01791	.01265
0.60	.00128	.00697	.00737	.00401	.00508
0.70	.00021	.00054	.00196	.00736	.00355
0.80	.00013	.00025	.00056	.00151	.00581
0.90	.00008	.00015	.00028	.00055	.00124

Table 35. Hematite extinction cross-section (μm^2) as a function of particle radius and wavelength.

	Particle radius (μm)				
λ(μm)	0.08	0.09	0.10	0.11	0.12
0.30	.05610	.04120	.06320	.08810	.17780
0.40	.09150	.12130	.07100	.12650	.09990
0.45	.10070	.11810	.15990	.07820	.13050
0.50	.15290	.12570	.14740	.17640	.10130
0.60	.02890	.12300	.20090	.18530	.21240
0.70	.01173	.02817	.08040	.29750	.25500
0.80	.00618	.01369	.02930	.06690	.21170
0.90	.00361	.00781	.01590	.03130	.06300

Table 36. Flux calculations at selected wavelengths and heights for aerosol and hematite concentration increased by 50% and 100%, and arbitrarily increased aerosol absorption coefficients by a factor of 2 and 3, leaving concentrations unchanged.

		Aerosol and hematite Concentration ·1.5			Aerosol and hematite Concentration ·2.0			β_{abs}^{aer} ·2			β_{abs}^{aer} ·3		
λ(μm)	H(m)	$F^{\uparrow}$	$F^{\downarrow}$	F_N	$F^{\uparrow}$	$F^{\downarrow}$	F_N	$F^{\uparrow}$	$F^{\downarrow}$	F_N	$F^{\uparrow}$	$F^{\downarrow}$	F_N
	8400	255	1035	780	252	1029	776	233	1037	804	212	1033	821
.42	2830	149	881	733	144	858	714	136	896	760	122	886	764
	300	74	673	598	67	609	542	73	716	643	66	690	624
	8400	292	1240	948	393	1235	942	262	1243	980	238	1240	1002
.47	2830	204	1101	897	200	1074	874	186	1119	934	167	1110	943
	300	130	879	749	120	804	685	129	932	803	119	905	786
	8400	291	1090	799	304	1087	783	249	1091	842	226	1090	864
.52	2830	236	1013	778	244	999	755	203	1022	818	183	1014	831
	300	168	884	716	165	838	673	157	907	750	145	882	737
	8400	248	919	671	258	917	659	215	921	705	195	919	724
.57	2830	212	862	650	216	849	633	187	870	683	169	864	695
	300	163	757	594	158	717	559	156	779	623	145	759	614
	8400	224	824	599	230	821	591	197	825	628	179	824	645
.62	2830	196	775	578	198	762	564	177	783	606	161	778	617
	300	159	680	521	152	642	490	155	703	548	145	686	541
	8400	199	720	521	205	718	513	175	721	546	159	720	561
.67	2830	177	683	506	179	673	494	159	690	530	146	686	540
	300	147	608	462	141	577	436	143	626	483	133	611	477
	8400	177	624	447	185	623	438	153	625	472	139	624	485
.72	2830	160	598	438	164	590	427	142	603	461	129	599	470
	300	132	542	411	129	519	390	126	554	428	118	541	423
	8400	160	597	387	166	546	379	139	547	409	126	547	420
.77	2830	146	526	380	149	519	370	129	529	400	118	526	408
	300	122	480	358	119	460	341	117	489	372	110	478	368
	8400	148	502	353	154	501	346	129	502	373	118	502	384
.82	2830	136	484	348	139	478	338	121	487	366	111	484	373
	300	115	443	328	112	424	312	110	451	341	103	441	338
	8400	133	438	305	138	437	299	116	438	322	106	438	331
.87	2830	122	423	300	125	418	292	110	425	316	101	423	322
	300	105	388	284	102	373	270	101	395	295	95	387	292

since the aerosol components vary with height, there may be a similar variation in the complex index of refraction. Figure 36 also shows the results of arbitrarily increasing the aerosol absorption coefficient by a factor of 2 and 3 while holding all other parameters constant. Increased net flux divergence results for all wavelengths.

In the previous results the contribution by hematite scattering has been neglected. Computations have therefore been performed which include hematite scattering along with (a) doubling the aerosol concentration while holding the hematite concentration constant, (b) doubling the hematite concentration while holding the aerosol concentration constant, and (c) doubling both aerosol and hematite concentrations. In these cases, the net flux divergence increases with increasing concentrations, providing better agreement with observations. However, the downward flux is then significantly reduced below observations and the upward diffuse flux is significantly increased above observations. It is concluded that the addition of hematite scattering provides poorer overall agreement with observational values.

The combined calculations provided in the sensitivity study show that calculations significantly overestimate the upward diffuse flux and underestimate the net flux divergence. More detailed theoretical calculations are necessary to determine the errors involved in the current theoretical phase function expansions. The remaining discrepancies would then be due to measurement errors.

It has been determined that aircraft roll fluctuations did not exceed 2° during the 10 seconds necessary to perform the spectral measurements. However, such errors may account for flux measurement variations of 5% for large zenith angles (54°). Furthermore, due to reflections

from the radiometer glass plate, incoming radiation at high angles is underestimated, particularly the diffuse flux. Errors in the upward-looking radiometer, where the solar beam is the major component of the measurement, are smaller than in the downward-looking instrument. This is particularly the case for conditions in which the diffuse flux is nearly isotropic. Under highly turbid or cloudy conditions in which the solar beam is very weak, then the upward-looking radiometer is also likely to provide underestimates of flux. Instrumentation errors of this kind for the highly turbid conditions encountered in the observations might (a) underestimate the downward flux in the lower layers, thereby indicating larger extinction and, therefore larger aerosol concentrations than actually observed, and (b) underestimate the upward flux. The result would be an overestimation of net flux divergences which are very sensitive to flux measurements. No estimates of the magnitudes of such errors are available at this time.

Finally, in order to determine the impact of aerosol upon the total radiation field, calculations for a "clean" atmosphere have been made with aerosol and hematite concentrations decreased by a factor of ten. The effect of the aerosol is to decrease the surface net flux by approximately 20% which leads to decreased surface heating. The upward diffuse flux is decreased by approximately 10% by the aerosol. The corresponding net flux divergence is increased by a factor of 10-15 by the aerosol.

PART IV. PROSPECTS FOR FUTURE STUDIES

The results from the present study indicate the very important influence of aerosols on the visible part of the spectrum. In particular, hematite (Fe_2O_3) was verified to be the strongest aerosol absorber of radiation and the dominant aerosol influence on the net flux. Indeed one sees that aerosol absorption exceeds gaseous absorption in some cases. Strong hematite absorption was also observed during the GATE experiment. These CAENEX results will aid in the evaluation of the GATE data where similar aerosol conditions were observed.

In the present investigation data were analyzed in the spectral region from 0.42 to 0.90 μm. It would now be appropriate to complete the solar spectrum by extending calculations to the regions 0.30 to 0.42 μm and from 0.90 μm to 3.00 μm. In addition, it is important to study the aerosol influence upon longwave radiative transfer. The spherical harmonics method described above is also available in the window region, 8-12 μm, for which data are also available.

The present research indicates how close cooperation between those involved in theoretical modelling and those involved in analysis of observational data can benefit both sides in providing deeper understanding of those parameters necessary for a complete and accurate description of the earth's radiation budget. In particular, actual data indicate where deficiencies in current models need to be improved as well as supply models with real data to simulate the real atmosphere. As predictive models and observations can be shown to converge, understanding of those physical parameters influencing radiative properties in the atmosphere increases and results in increased confidence in model

predictions. Likewise comparison of accurate theoretical models with observational data helps those involved in field studies better appreciate which data are critical for proper evaluation of the radiation field and where increased resolution is required.

One of the most important results of this interaction has been to familiarize the various groups with the data and requirements which each of them share and contribute.

One great difficulty which has been exposed in the present interaction is the lack of standardized data among the various parties involved. Future efforts will be directed towards such a standardized data format in order to facilitate utilization of the data.

As seen in the results, the greatest problems seem to be associated with measurements of aerosol concentration, size distributions, chemical composition and optical properties. In addition, there is a lack of adequate gaseous concentration measurements and a lack of sufficiently reliable data on gaseous absorption coefficients in the visible region. A more difficult problem is to determine the aerosol properties and concentrations in the upper troposphere and lower stratosphere. These regions show large relative disagreements between measured and calculated values.

Further intercomparisons between the observational data from different CAENEX expeditions and the results of numerical modelling sould be valuable. Observations for urban conditions and GATE observations of the Saharan dust with strong hematite concentrations are of particular interest.

In each of the regions of interest it would be of particular value to consider the following cases:

1) "clean" atmosphere; background or light aerosol conditions and cloudless skies,
2) "clean" atmosphere with clouds,
3) polluted atmosphere; turbid conditions,
4) polluted conditions with clouds.

At the first stage of analysis of cloudy conditions, it is important to consider only horizontally homogeneous layer clouds. Broken cloud conditions require statistical or Monte Carlo calculations which are much more computationally expensive.

More extensive size distribution calculations as a function of height are expected to be significant. However, it was not possible during the present investigations to consider the impact of different size distributions since the more important aerosol concentrations are known inadequately. Finally, the impact of relative humidity upon aerosol optical properties must be included for relative humidities exceeding 60%.

More extensive measurements of the parameters characterizing atmospheric dynamics during the radiation measurements would be extremely valuable. In particular, recent measurements in urban regions indicate that heavily polluted air tends to maintain those inversions, which are responsible in turn for strong pollution episodes. Recent theoretical investigations[20] indicate that such inversions may affect surface temperatures by as much as 10-15° C compared to non-polluted conditions. A set of observations made several times during the day would provide a sufficient data base to examine the magnitude of such effects.

PART V. CONCLUSION

In conclusion, the following short summary of recommendations for future complex investigations can be made.

(1) The impactor appears to have been saturated leading to underestimates of the aerosol concentrations and probable errors in the size distribution. Such effects will lead to erroneous optical characteristics. Perhaps this defect can be overcome by using a continuously moving collector plate so as to smear the incoming particles and thereby allow for more accurate particle counts.

(2) It is necessary to determine size distributions for highly active substances such as hematite. It is not sufficient to merely determine the percentage of total aerosol and assume either identical size distributions or delta function distributions.

(3) A thin foil impactor or some other device would be most useful to determine liquid water contents and size distribution functions under moist and cloudy conditions.

(4) The radiometers should be recalibrated.

(5) Since it requires 12 seconds to make one complete spectral measurement during which the aircraft platform may roll appreciably, at least several minutes worth of data at each altitude are required to reduce flux measurement errors.

(6) A determination of errors associated with underestimates of incoming radiative flux at high angles to the radiometers should be made. Such errors may be particularly significant in near isotropic conditions.

(7) Data should not be smoothed, interpolated, or extrapolated. Data should be clearly labelled as to the exact time and height at which it was taken. If aerosol data are taken through a layer, then the height ranges should be indicated.

(8) Theoretical calculations should be checked in order to determine the errors associated with the current theoretical phase function expansions.

(9) There should be closer cooperation among the scientists working on different components of the observational program to insure that aerosol measurements correlate with flux measurements.

It can be seen that such intercomparison studies can be beneficial to both the experimentalist and the theoretical modeller in helping to better understand the earth's atmospheric energy budget. Therefore, more extensive and complete field studies, improved instrumentation, and further intercomparison studies under a variety of conditions are indicated. In future work these studies will be extended to a broader spectral interval.

The experience acquired during the CAENEX and GATE experiments as well as the results obtained from calculations have been fully considered in working out the Global Atmospheric Aerosol-Radiation Experiment (GAAREX) proposal. It is hoped that this report will provide additional insight into the requirements for successful radiation transfer observations in real atmospheres.

The authors express their sincere gratitude to M.A. Prokofyev and to Edward Sorokin.

REFERENCES

1. "Complete Atmospheric Energetics Experiment (CAENEX-70 expedition data), MGO Proceedings, Vol. 276, pp. 279, GIDRO Meteorizdat, Leningrad, 1972.

2. "Complete Atmospheric Energetics Experiment (CAENEX-71), MGO proceedings, 1973, Vol. 296, pp. 140.

3. "Complete Atmospheric Energetics Experiment (results of research, 1970-1972)", MGO Proceedings, 1973, Vol. 322, pp. 84.

4. Kondratyev, K.Ya., "Complete Atmospheric Energetics Experiment (CAENEX)", VNIIGMI - MCD, Obninok, 1973, pp. 79.

5. "Complete Radiation Experiment" edited by K.Ya. Kondratyev and N.E. Ter-Markaryants, Gidrometeoizdat, Leningrad, 1976, pp. 240.

6. Kondratyev, K.Ya., et al., "Aerosol impact of radiation transfer - possible climatic effects", Leningrad State University publication, 1973, pp. 266.

7. "Research in Atmospheric Radiation" MGO Proceedings, Vol. 317, 1973, pp. 156.

8. Kondratyev, K.Ya., and O.B. Vasilyev, "Die Bedentung des Aerosols fur den Strahlungshaushalt und sein moglicher Eingluss auf das Klime", Zeitsehrift fur Meteorologie, Heft 3, Band 25, 1975, p. 129-142.

9. Vasilyev, O.B. and V.V. Fedorov, "Vertical Profiles of free atmosphere spectral optical parameters over the desert", Problems of Atmospheric Physics, Issue 13, Edited by K.Ya. Kondratyev, Leningrad State University Press, pp. 33-75.

10. "Complete Atmospheric Energetics Experiment (CAENEX-73)", MGO Proceedings, 1975, Vol. 366, pp. 98.

11. "Radiative Characteristics of the Atmosphere and the Earth's Surface", Edited by K.Ya. Kondratyev, Gidrometeorizdat, Leningrad, 1969, pp. 564.

12. M. Zdunkowski, W.G. Korb, "An approximative method for the Determination of shortwave radiative fluxes in Scattering and Absorbing Media", Contributions to Atmospheric Physics 47, 1974, pp. 129-144.

13. Welch, R., J.F. Geleyn, G. Korb, and W. Zdunkowski, "Radiative Transfer of Solar Radiation in Model Clouds", to appear in Contributions to Atmospheric Physics, 1976.

14. Korb, G.J., R.M. Welch and W.G. Zdunkowski, "An approximative method for the determination of Infrared Radiative Fluxes in Scattering Absorbing Media", Contributions to Atmospheric Physics, 48, 1975, pp. 85-94.

15. Welch, R. and W. Zdunkowski, "A radiation model of the polluted Atmospheric Boundary Layer", to appear in the Journal of Atmospheric Science, November, 1976.

16. Canosa, J., and H.R. Penafiel, "A direct solution of the Radiative Transfer Equation: Application to Rayleigh and Mie Atmospheres". J. Quant. Spectrosc-Radiat. Transfer, 13, 1973, pp. 21-39.

17. Dave, J.V. and J. Canosa, "A direct solution of the Radiative Transfer Equation: Application to Atmospheric Models with Arbitrary Vertical Nonhomogeneities", JAS, 31, 1974, pp. 1089-1101.

18. Deuze, J.L., C. Devaux, and M. Herman, "The Spherical Harmonics Method for radiative transfer computations. An extension for some inhomogeneous atmospheres", Nouv, Rev. Optique 4, 1973, pp. 307-314.

19. Liou, K, "A numerical Experiment on Chandrasekhar's Discrete-Ordinate Atmospheres. JAS, 30, 1973, pp. 1303-1326.

20. S. Chandrasekhar, Radiative Transfer, New York, Dover Press, 1950.

21. Putzer, E.J., "Avoiding the Jordan canonical form in the discussion of linear systems with constant coefficients", Amer. Math. Monthly, 73, 2, 1966.

BIBLIOGRAPHIC DATA SHEET	1. Report No. CSU-ATS-261	2.	3. Recipient's Accession No.

4. Title and Subtitle	5. Report Date
Comparison between the measured and calculated spectral characteristics of shortwave radiation in the free atmosphere over the desert (from the data of the CAENEX-70 expeditions),	December 1976
	6.

7. Author(s)	8. Performing Organization Rept. No.
K. Ya. Kondratyev, R.M. Welch, O.B. Vasiliev, V.F. Zhvalev, L.S. Ivlev, V.F. Rodionov.	

9. Performing Organization Name and Address	10. Project/Task/Work Unit No.
Colorado State University, Dept. of Atmospheric Science, Fort Collins, Colorado 80523, USA. Leningrad State University. Main Geophysical Observatory, Leningrad, USSR.	11. Contract/Grant No. ATM 76-21348 ATM 76-06178

12. Sponsoring Organization Name and Address	13. Type of Report & Period Covered
National Science Foundation, Washington D.C. 20550, USA. Hydrometeorological Service of the USSR, Moscow, USSR.	Research Report November 1975-November 1976
	14.

15. Supplementary Notes This contribution is one of a series of reports which will be published jointly as CSU Atmospheric Science Papers and in the Transactions of the Main Geopysical Observatory, USSR.

16. Abstracts

The report presents a summary of a joint Soviet/American exchange program to compare calculations with observations in the real atmosphere, in order to determine and study the diabatic processes that are important for tropospheric energetics. Radiative transfer calculations have been performed using complete spectral measurements of the radiation field and aerosol optical properties under turbid conditions. The effect of a small amount of highly absorbing material, such as hematite, is demonstrated, and theoretical results are discussed. Extensive data are presented giving spectral shortwave radiation flux and flux divergence values as a function of height in the atmosphere. Because no "best fit" over all spectral regions was possible further studies were performed to test the sensitivity of the results to small variations in the input parameters. Preliminary findings indicate that size distributions for the various components of the aerosol, especially hematite, should be provided.

17. Key Words and Document Analysis 17a. Descriptors

Radiative Transfer Calculations
Aerosol
Desert
Hematite
Real Atmosphere
Soviet/American Exchange Program
CAENEX

17b. Identifiers/Open-Ended Terms

17c. COSATI Field/Group

18. Availability Statement	19. Security Class (This Report) UNCLASSIFIED	21. No. of Pages 79
	20. Security Class (This Page) UNCLASSIFIED	22. Price